

Part II

Chapter 7

The ALICE experiment

7.1 Introduction

ALICE (A Large Ion Collider Experiment) [152] is the dedicated heavy-ion experiment designed to exploit the unique physics opportunities which will be offered by nucleus-nucleus collisions at the LHC. ALICE is going to study nuclear matter under extreme conditions of energy density, at a centre-of-mass energy per nucleon pair of 5.5 TeV. The physics motivation is the study of QGP in a new energy regime and characterizing it in particular by so-called ‘rare probes’.

The ALICE detector is conceived as a general-purpose detector, sensitive to the majority of known observables including hadrons, electrons, muons and photons. It will allow the study of a number of specific signals in the same experiment together with global information about the events. The observables accessible include:

- global event features;
- production cross-section of J/Ψ and Υ families coupled with the measurement of D and B mesons;
- prompt photons and lepton pairs;
- cross-section of high- p_T hadrons;
- strangeness production;

- multiplicity fluctuations;
- particle correlation;
- particle ratios and transverse-momentum distributions.

The LHC will start to collide protons at $\sqrt{s} = 14$ TeV in the middle of 2007 and will provide the first heavy ion collisions (Pb–Pb) at the end of its first year of operation at $\sqrt{s} = 5.5$ TeV.

7.2 The ALICE detector layout

The estimated high multiplicities (up to 8000 charged particles per rapidity unit), the relatively low event rate which will characterize Pb–Pb collisions at LHC and the need of a large acceptance for event-by-event analysis and HBT interferometry play a crucial role in the design of ALICE.

The strategy of ALICE is to combine a nearly exclusive measurement of particle production in the central region with spectroscopy of quarkonia state at central and intermediate rapidities and global event characterization. Therefore the experimental setup combines three major components: (a) the central barrel, contained in the L3 magnet, where most charged particles are detected including electron identification and photon measurements; (b) the forward muon spectrometer [23], dedicated to the study of muon pairs from quarkonia decays in the interval $2.5 \leq n \leq 4.0$; and (c) the forward detectors, dedicated to global event characterization based on photon and charged particle multiplicity counters and forward calorimetry.

A longitudinal view of the ALICE detector is shown in Fig. 7.1. The central barrel detectors cover $\pm 45^\circ$ ($|\eta| \leq 0.9$) over the full azimuth and are embedded in a large magnet with a solenoidal field up to 0.5 T, where the charged particle tracking is performed. Tracking starts in the Inner Tracking System (ITS), with six layers of high-resolution silicon detectors, located around the interaction point, for precision tracking and primary as well as secondary vertex reconstruction; it extends the central barrel acceptance for multiplicity measurements up to $|\eta| < 2.0$. It is followed by a large Time Projection Chamber (TPC), the

main tracking device, for momentum determination and particle identification via dE/dx . A layer of Transition Radiation Detectors (TRD), for electron identification, enhances in addition the tracking capabilities at high- p_T and is used for high- p_T triggering. Hadrons are identified via dE/dx in the TPC and ITS in the range $\sim 100 - 550$ MeV/c, and up to ~ 900 MeV/c for protons. A Time-Of-Flight array (TOF) over the TPC geometrical acceptance provides hadron identification in the intermediate p_T range, while high- p_T is covered over a limited acceptance at mid-rapidity by an array of ring-imaging Cherenkov counters, the High Momentum Particle Identification Detector (HMPID): up to 3 GeV/c for K/π and up to 5 GeV/c for p/K separation. Photons and neutral mesons are measured in the electromagnetic calorimeter (PHOS). This central barrel will be complemented at pseudorapidities of $2.5 \leq \eta \leq 4.0$ by a muon spectrometer with a dipole magnet and finally an iron wall to select muons.

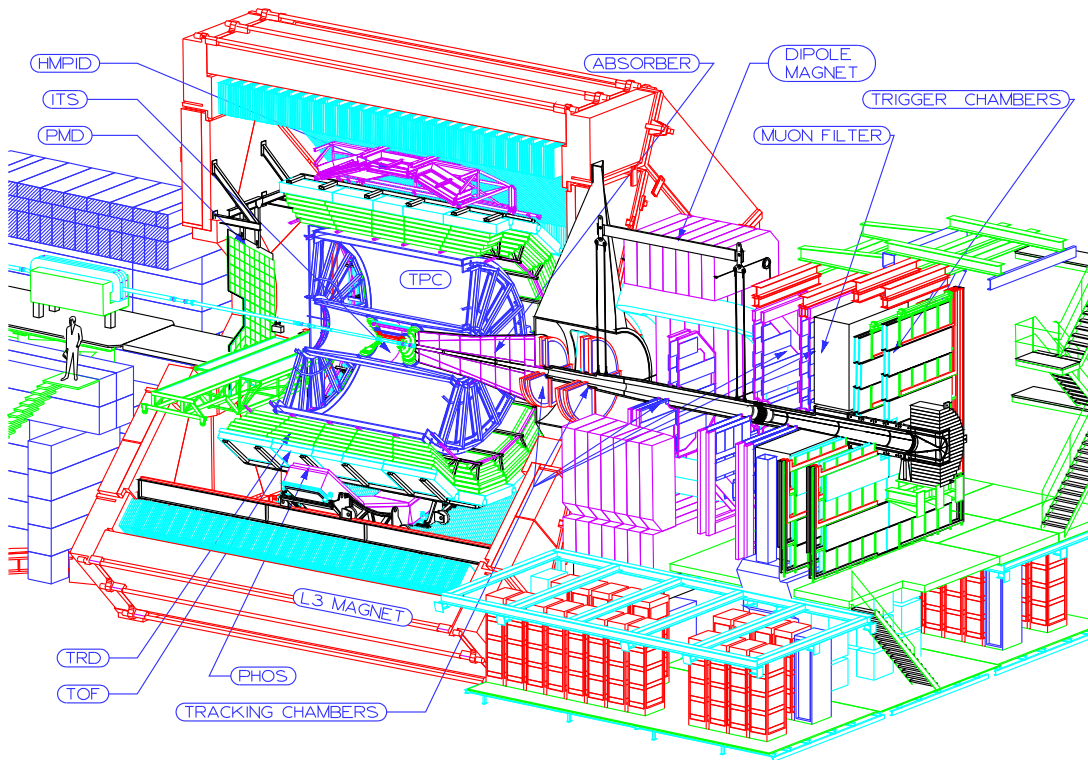


Figure 7.1: Longitudinal view of the ALICE detector.

7.3 Studies of gas properties for the ALICE central detectors

ALICE will consist of large-volume gaseous detectors which are expected to operate continuously for a long period of time. The design of these detectors is optimized with the precise knowledge of their gas properties as well as of the radiation load on their various parts.

In the next two chapters we study the drift velocity and gain in argon- and xenon-based mixtures and estimate the radiation background in the ALICE TRD.

Chapter 8

Drift velocity and gain in argon- and xenon-based mixtures

Measurements of drift velocities and gains in gas mixtures based on Ar and Xe, with CO₂, CH₄, and N₂ as quenchers, are presented. The dependence of Ar- and Xe-CO₂ drift velocities and gains on the amount of nitrogen contamination in the gas is also shown. In addition, a quantification of the Penning mechanism which contributes to the Townsend coefficients of a given gas mixture is proposed. The measured velocities are compared with calculations using the Magboltz code.

8.1 Introduction

For ionization detectors, an understanding of the motion of the electrons and ions in gases is extremely important as these factors influence many operating characteristics of the detector. For the most part, this motion is described by the classical kinetic theory of gases. In the presence of an electric field, the electrons and ions freed by radiation are accelerated along the field lines towards the anode and cathode respectively. This acceleration is interrupted by collisions with the gas molecules which limit the maximum average velocity which can be attained by the charge along the field direction. The average velocity attained is known as the *drift velocity* of the charge and is superimposed upon its normal random movement.

The *drift velocity* u_D in an electric field is given by :

$$u_D = \frac{e\tau E}{2m} \quad (8.1)$$

Where e is the charge, E is the electric field, m is the mass of the particle and τ is the mean time between the collisions. Compared to their thermal velocities, the drift speed of the ions is slow, however, for electrons this can be much higher since they are much lighter. In position sensitive ionization detectors, u_D is typically arranged to be of the order of several cm/ μ s.

The essential component in a drift chamber is usually one of the noble gases (such as argon or xenon) plus a second component, the quencher, which could be any other gas with large number of degrees of freedom, such as poly-atomic or organic compounds. The addition of a quencher fraction to a noble gas increases the macroscopic drift velocity u_D of free electrons and decreases the diffusion at a given drift field, temperature and pressure.

Modern detectors such as those being constructed for the Large Hadron Collider (LHC) include large-volume gaseous detectors which are expected to operate continuously for several months every year. The design of these detectors and their read-out electronics can be optimized with precise knowledge of the drift velocity and of the gas gain. These relevant gas parameters depend on the detector field configuration and on the gas components, composition, density, and purity.

The ALICE Transition Radiation Detector (TRD) will be used for electron identification and particle tracking in the high multiplicity environment of heavy-ion collisions at LHC. This requires accurate pulse height measurements in drift chambers filled with Xe, CO₂ (15%) gas mixture over the drift time of the order of 2 μ s. Details related to the development of the ALICE-TRD Readout Chambers as well as to the required gas mixture and its properties can be found in [85, 86]. Due to the large volume (28 m³) of this barrel detector and the high cost of xenon, the drift gas will be recirculated in a closed loop, with a modest rate of fresh gas injection. A certain fraction of contamination (O₂, N₂, H₂O) is entering into the gas volume through leaks. While oxygen can be readily removed by appropriate filters, the known methods for nitrogen removal are complex and tedious, and lead to further losses of the main gas and to the modification of its composition. The latter circumstance is particularly undesirable during data

taking periods. Thus, nitrogen gradually builds up into the mixture. After a running period of 8 months, the nitrogen content of the TRD gas rises up to 8 % and can be cryogenically distilled and removed from the mixture during the shutdown periods, at a moderate loss of xenon.

The needs of the ALICE TRD xenon-based gas mixture in terms of regeneration from nitrogen contamination are discussed in [76]. We have shown that the separation of N_2 from Xe- CO_2 mixture by cryogenic distillation performs satisfactorily. Most of the nitrogen has been successfully removed from the mixture at a moderate loss of xenon. Two existing cryogenic plants have been thoroughly tested and nitrogen levels down to 1% have been achieved. During the running time, the increasing amount of nitrogen influences the drift velocity. Therefore, systematic studies of the influence of N_2 on the gas properties become very important.

We have also performed measurements [77] of pulse height distributions in drift chambers operated with Xe, CO_2 mixtures. After studying the general behavior of these distribution under clean conditions, we have investigated the effect of oxygen and SF_6 contamination on the detection gas. A small signal loss due to attachment is seen for O_2 impurities up to a few hundred ppm. In case of SF_6 , a contamination even at the level below 1 ppm produces a dramatic loss of signal over the drift length of about 3 cm. Attachment on SF_6 is studied here for the first time concerning its practical implications for gas detectors. As the SF_6 was found accidentally in some xenon supplies, it is important to have a careful monitoring of the SF_6 contamination when precision measurements are performed using Xe-based gas mixtures in drift chambers. We have used ECD gas chromatography analysis to detect and quantify small traces of SF_6 . We have shown that measurements of ^{55}Fe signals in monitor detectors are very sensitive to SF_6 contamination, thus allowing an inexpensive in situ check of the gas quality. Thus, using xenon supplies as SF_6 -free as possible is an important requirement. In the following we used clean xenon.

The experimental set-up which is used to measure both the drift velocity and the gain of various gas mixtures, is described in the next section, followed by the measurement procedure. In section 8.3 the measured drift velocities are shown. Measurements of drift velocities in some binary and ternary Xe-based mixtures

(without nitrogen) have been published earlier [87, 88, 89, 90]. The results are compared to existing data where available and to simulations, in order to validate our method. The gain measurements, together with results from simulations, are presented in section 8.4. We finally draw our conclusions.

8.2 Experimental setup

Several methods have been described in the literature to measure drift velocities in gases [78, 79, 80, 81, 82, 83, 84]. They differ in the technique applied to generate free electrons. In some setups electrons are released from a photocathode through illumination with UV light or from radioactive β -sources, like ^{90}Sr . In recent experiments UV-laser beams are widely used to ionize molecules in the gas mixtures. The experiments also vary in the way they measure the drift time of the electrons.

In the present work, we have chosen a small drift chamber with a geometry similar to that anticipated for the final ALICE TRD [85], but with a much smaller active area ($10 \times 10 \text{ cm}^2$). The chamber has a drift region of 31.5 mm and an amplification region of 6.4 mm. The anode wires (W-Au, 20 μm diameter) have a pitch of 5 mm. For the cathode wires (Cu-Be, 75 μm diameter) the pitch is 2.5 mm. The signal is read out on a cathode plane segmented into rectangular pads of area 6 cm^2 each. The drift electrode is made of a 25 μm aluminized Kapton foil, which also serves as gas barrier. The electric field thus created is sufficiently uniform over the full active area of the pad plane. The mass flowmeters were calibrated for each gas mixture.

A schematic view of the set-up used for the drift velocity measurements is shown in Fig. 8.1. Two sets of slits, 0.75 mm wide, are machined into the stesalit side walls of the drift region and covered with Kapton foils. Electrons from a collimated ^{90}Sr radioactive source enter the drift volume through either of these slits, and ionise the gas. Some of these particles cross the corresponding slit at the other side of the drift enclosure, behind which a scintillator is placed for triggering purposes. Triggered events will show signals in the 8 pads, with a drift time corresponding, on average, to the distance from the selected set of slits to the anode plane. A 2 mm thick lead absorber is placed behind the opposite outlet

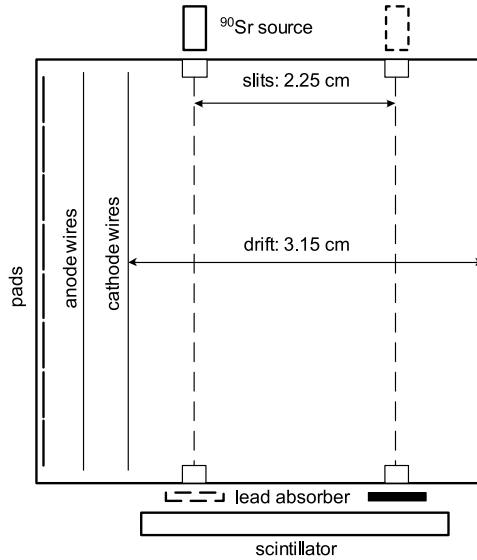


Figure 8.1: Schematics of the modified drift chamber used for the drift velocity measurements.

slit to prevent triggers from particles going at an angle through the detector. For each set of slits, we record on FADCs the pulse height distributions on the pads as a function of the drift time of the tracks. The corresponding average times are evaluated and then subtracted for a constant value of the electric field as it is shown in Fig. 8.2. Measuring the arrival time difference Δt and knowing Δx , provides $u_D = \Delta x / \Delta t$, the drift velocity component parallel to the electric field E . In this way, the contribution to the drift time of the amplification region, where the electric field is not uniform, is cancelled. The anode voltage is adjusted for each mixture to achieve a gain near 10^4 , and ranges between 1450 V and 1800 V. Both the pad plane and the cathode wires are kept at ground potential. The amplification field leaks through the cathode wire plane and effectively increases the drift field. In order to correct for this effect, the position of the 0 Volts equipotential line, relative to the position of the cathode wires, is computed with the Garfield simulation package [91] for each set of anode and drift voltages. This shift, which depends on both the drift and anode voltages, ranges in our case from 0.02 mm to 6 mm. The reduced electric field is finally evaluated taking

into account the recorded atmospheric pressure. The oxygen and water vapour in the gas was monitored during the measurements, and varied, depending on the gas flow, between 10 and 50 ppm O₂, and 300 to 500 ppm H₂O. This experimental set-up allows the determination of electron drift velocities as a function of the reduced electric field E/p with a systematic uncertainty estimated to be lower than 10 % .

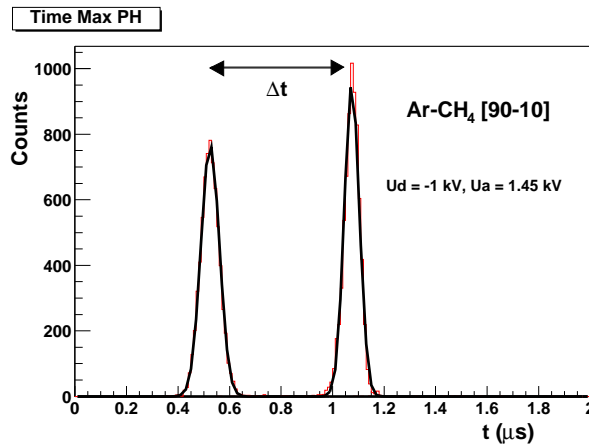


Figure 8.2: Pulse height distributions on the pads as a function of the drift time.

We use a prototype of the charge-sensitive preamplifier/shaper (PASA) especially designed and built for TRD prototypes with discrete components. It has a noise on-detector of about 2000 electrons r.m.s. and the FWHM of the output pulse is about 120 ns for an input step function. The nominal gain of the PASA is 3 mV/fC. The FADC has an 8-bit non-linear conversion and adjustable baseline, and runs at 100 MHz sampling frequency.

8.3 Drift velocity measurements

In order to check and validate how reliable is the experimental method we used, we first measured the drift velocity of a well known mixture, Ar-CH₄ [90-10], and compared our results with existing data [90] that we refer to as MIT data. We also compare the measurements with Magboltz [93] calculations. Magboltz is a simulation program, which calculates electron transport parameters such as

drift velocity, diffusion coefficients, Lorentz angle and electron energy for arbitrary values of electric and magnetic fields. Input parameters are temperature, pressure, electric and magnetic field settings and composition of the desired gas.

Our results are compared without and with the correction of the reduced field due to the leakage of the anode field into the drift region. This correction is higher at lower drift fields. As can be seen in Fig. 8.3, the agreement between this work and the calculation is good only after the correction of the drift field values. On the other hand, a clear discrepancy with the MIT data is visible at low fields, and reaches 10 %. The argon data showed no difference, within 2 %, in the results obtained from any pad, meaning that the drift field is uniform enough in the regions above the pads at the edges of the active area.

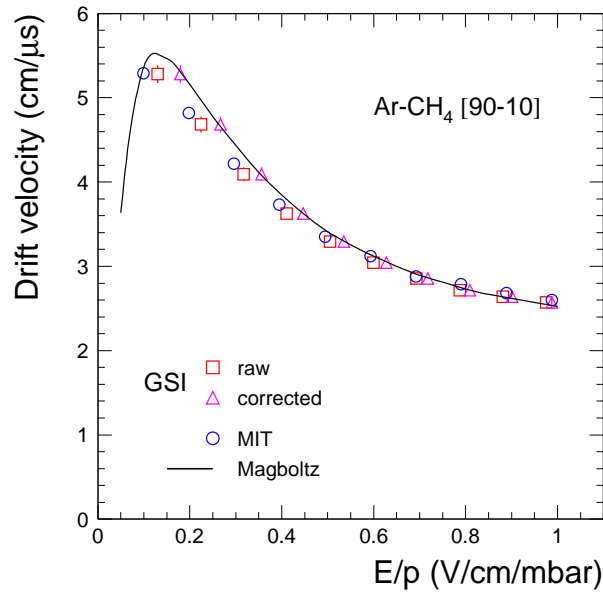


Figure 8.3: Drift velocity measurements and calculations in Ar-CH₄ [90-10]. The effect of the anode potential on the configuration of the electric drift field manifests itself (square data points) especially at low fields, and is corrected for (triangles).

In case of xenon mixtures, we should expect a significant multiple scattering of electrons coming from the ⁹⁰Sr source. To evaluate this effect, we measured the

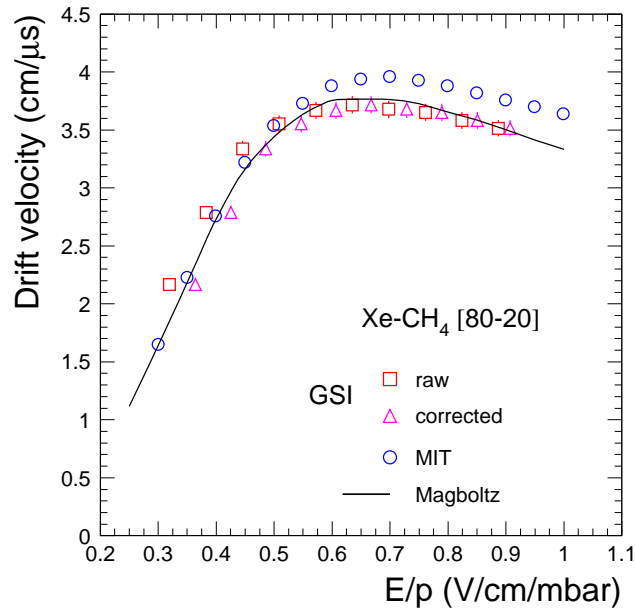


Figure 8.4: Drift velocity in Xe-CH₄ [80-20], with (triangles) and without (squares) drift field correction as measured in this work, together with other measurements and a calculation.

drift velocity of Xe-CH₄ [80-20], which the MIT group has also measured. We have observed that the multiple scattering, combined with the asymmetric gas volume available for tracks emerging from either slit, biases the measurement towards larger drift velocities by, in this case, as much as 15 %. In order to avoid that overestimation, we work with drift time distributions measured on the pad closest to the entrance slit only, for which multiple scattering is minimal. The resulting drift velocity and its comparisons are shown in Fig. 8.4.

There is again a significant discrepancy between our measurement and the MIT results at fields above drift velocity saturation. However, the calculations of the drift velocity in this region are compatible with our measurements. At low fields, on the contrary, the MIT data agree well with the calculation, whereas our results underestimate the calculated values by 7 % near 0.45 V/cm/mbar.

The next set of measurements were undertaken for Ar-CO₂ [85-15] and admixtures of 0, 10 and 20 % N₂. Adding, for example, 10 % N₂ into the mixture

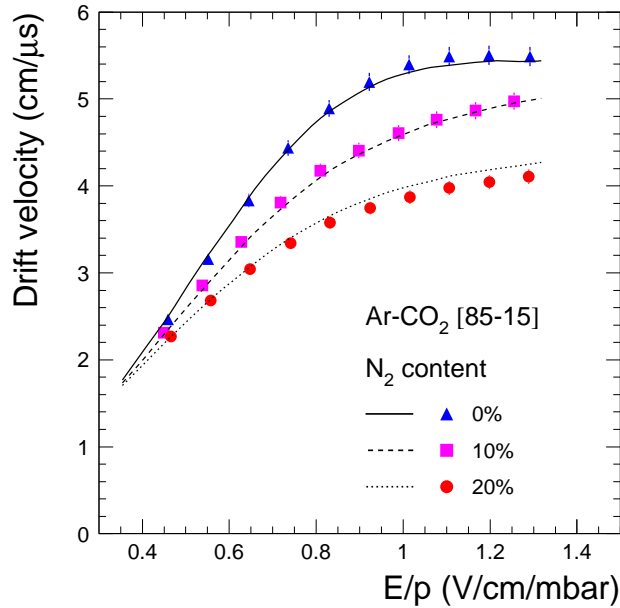


Figure 8.5: Drift velocity in Ar-CO₂ [85-15] with N₂ additions. The measurements (symbols) are compared to simulations (lines).

results in an Ar-CO₂-N₂ [76.5-13.5-10] mixture. As can be seen in Fig. 8.5, the drift velocity decreases with increasing concentration of nitrogen, and there is a reasonable agreement between measurements and simulation. Due to the saturation of the drift velocity at lower values with increasing N₂ content, keeping the drift velocity constant would require higher and higher drift voltages as the gas composition changes, and to maintain a fast mixture would eventually become impossible.

Finally, the results for Xe-CO₂ [85-15] mixtures with 0, 10 and 20 % N₂ admixtures, shown in Fig. 8.6, exhibit a weak dependence on the nitrogen concentration. We notice deviations of up to 12 % with respect to the calculations at intermediate fields. The calculated drift velocities exhibit a crossing of the three curves at a field near 800 V/cm. The measurements show very little dependence of the drift velocity on the N₂ concentration at fields up to this value. Since, for example, the anticipated electric field of the ALICE TRD is 700 V/cm, this circumstance should be welcome: no large drift velocity variation is expected due

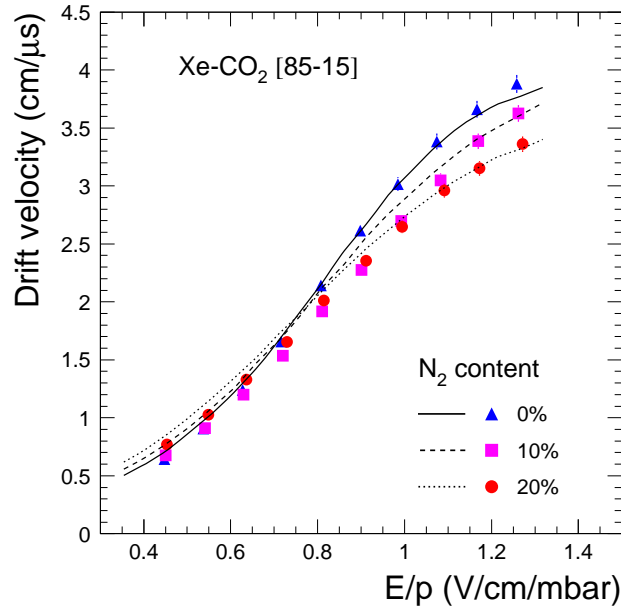


Figure 8.6: Drift velocity in Xe-CO₂ [85-15] with N₂ additions.

to substantial accumulations of nitrogen.

8.4 Gain measurements

The gain is measured with an ⁵⁵Fe source, by counting the number of signals produced by X-rays absorbed in the gas, and measuring the currents drawn by the anode high voltage power supply due to these photons. Typical rates are 60 kHz in a projected area of order 1 cm². The number of primary electrons per photon produced in the gas is derived for each mixture separately using the work functions given in [92]. The drift voltage during these measurements was set at -2 kV.

The general formula that we used to estimate the *Gain* G in an electric field is given by :

$$G = \frac{I(nA)}{Rate_{Fe}(Hz) \times Ne \times 1.6 \times 10^{-10}(nA/e^-)} \quad (8.2)$$

Where I is the measured current in the detector, $Rate_{Fe}$ the number of signals

produced by X-rays absorbed in the gas, Ne the number of primary electrons per photon produced in the gas¹ (if W is the energy needed to release a free electron and $E_{Fe}=5.96$ keV, $Ne^- = E_{Fe}/W$).

As explained above, the absolute gain as a function of the anode voltage is measured with the use of a ^{55}Fe source, which is placed in front of the entrance window of the chamber. We have also carried out calculations of the gain with the use of the package Magboltz 2 [93]. This program computes the Townsend and attachment coefficient for a given gas mixture and electric field. By introducing this information, together with the chamber geometry and voltages, into Garfield [91], one can calculate the gain of the detector for each mixture and anode voltage. The multiplication factor obtained in this way accounts for the electrons produced in the avalanche by collisions of atoms or molecules with other energetic electrons. In addition, Magboltz 2 provides information about the excited and ionised species produced in the avalanche. This information can be used to scale up the Townsend coefficients, according to the ionisation of gas species due to collisions with other excited metastable gas states (Penning effect) [94, 95, 96]. Since this energy transfer rate is a priori not known, the experimental data are used as a guide to tune one parameter, the so-called Penning fraction, for matching the calculations to the measurements. The Penning fraction refers to the amount of a given excited species which effectively ionise an atom or molecule, normalised to the abundance of such species and provided the energy balance of the process allows for the reaction. It should be noted, though, that this parameter is unique for a given gas mixture, i.e. it does not depend on the electric field nor the high voltage, and that it is expected to vary according to the characteristics of the quencher(s) and noble gas used in the mixture. In other words, the Penning transfer can be regarded as a measure of how well a quencher works: light noble gases tend, through their excited states, to ionise quenchers such as CO_2 , and therefore the Penning fraction in these mixtures are expected to be relatively large. On the other hand, heavy noble gases will tend to be ionised, probably to a lower extent, by excited molecules of certain quenchers (Penning mixtures).

¹The numbers of primary electrons for different gas components are [92] : $Ne_{Ar} = 227$, $Ne_{Xe} = 268$, $Ne_{N_2} = 169$, $Ne_{CO_2} = 179$

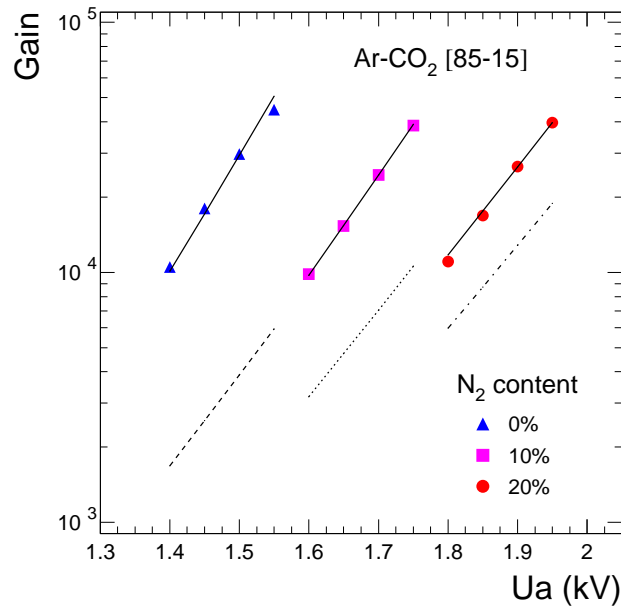


Figure 8.7: Gain in Ar-CO₂ [85-15] with N₂ additions. The dotted lines are calculations with Magboltz 2 and no Penning transfer. The tuning of the Penning transfer parameter to the data yields 37, 20, and 8 %, for 0, 10, and 20 % N₂, respectively (solid lines).

In the case of Ar-CO₂-N₂ mixtures, the suggested Penning mechanism to provide extra gain is the reaction $\text{Ar}^* + \text{CO}_2 \rightarrow \text{Ar} + \text{CO}_2^+ + e^-$, where the average excitation energy of the Ar D-levels is 14.0 eV and the ionisation potential of CO₂ is 13.773 eV. Fig. 8.7 shows the measured and calculated gain as a function of anode voltage for the three argon-based mixtures. As can be observed, after tuning of the Penning fraction to the second highest point in each curve, the slopes are properly matched by the calculations. The Penning fraction decreases from 37 % in the case of no nitrogen to 8 % when the N₂ admixture is 20 %. This means that nitrogen limits the Penning ionisation of CO₂. This effect may occur by quenching of the excited argon states by N₂ or by the occasional excitation of the nitrogen molecule thus leaving the argon atom unexcited. The highest excitation level in N₂ used in the calculations corresponds to 13.0 eV. The difference in voltage for equal gain in this series of mixtures is about 200 V, and apparently

this gap increases with the gain.

Shown also in Fig. 8.7 are the calculated gains with no Penning effects, which fail to reproduce the measurements. In addition, the slopes, at least for the nitrogen free case, are less steep than the experimental ones, and the disagreement of the calculations with the measurements decreases with increasing N_2 concentrations. Thus, the effect of nitrogen in this mixture, apart from lowering the gain at a given voltage, is to reduce the Penning effect by providing more effective quenching.

The case of the Xe-CO₂-N₂ mixtures is, from the Penning transfer point of view, different from argon. In this case, the highest energy level of excited Xe is 11.7 eV, insufficient to ionise CO₂. Levels in CO₂ between the Xe ionisation energy, 12.13 eV, and the CO₂ ionisation at 13.773 eV have sufficient energy to cause xenon ionisation. Unfortunately, due to the lack of data, all CO₂ excitations above 10.5 eV have been combined into a single level at 10.5 eV [97, 98] in the simulation program. This does not exclude an analysis similar to the previous mixture since only a fraction of the excitation of the 10.5 eV level representing levels above 12.13 eV are used in the simulation. In conclusion we assume that the Penning transfer occurs from CO₂^{*}(10.5) onto ionisation of xenon. The effect of N₂ on the Xe-CO₂ mixture is quite complex. There are possible energy transfer channels from CO₂^{*} to N₂ as in the Ar-CO₂ mixture but also from N₂^{*} to ionisation of Xe. The nitrogen excited states are produced less copiously than the CO₂ excited states according to calculations done with Magboltz 2. Therefore as an approximation we assume the dominating transfer is from CO₂^{*} to Xe.

As can be seen in Fig. 8.8, the experimental gain measurements, and the calculations performed under these assumptions, give an approximately constant Penning fraction (22 %). All slopes are correctly reproduced, with and without Penning transfer. The voltage gaps between the curves is about 50 Volts. The deviation of the data from the calculation -tuned at the middle point of each curve- at high gains is probably an indication of space charge effects within the amplification region due to the high X-ray rates. It is interesting to note that this measured deviation from exponential behaviour seems to decrease with increasing N₂ concentration, probably due to the higher anode fields involved. This also implicates space charge as the cause.

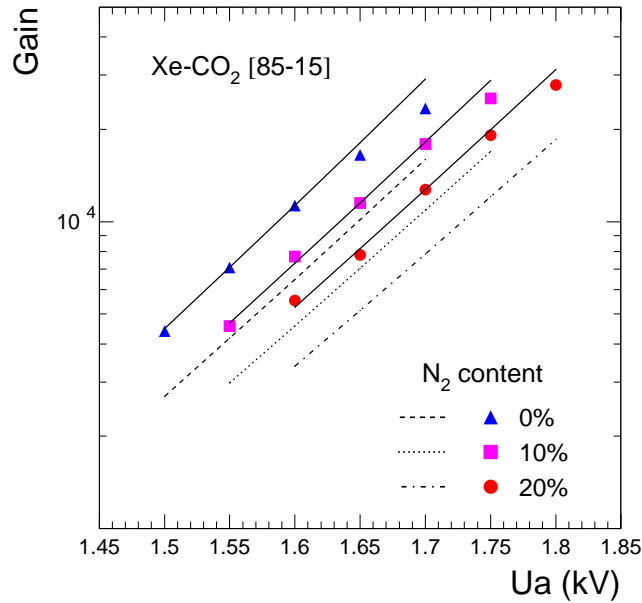


Figure 8.8: Gain in Xe-CO₂ [85-15] with N₂ additions. The tuned Penning transfer rates are 24 % for the N₂-free mixture, and 22 % for the mixtures with N₂.

8.5 Conclusions

Drift velocity and gain measurements have been performed for a number of gas mixtures in order to assess the effect of nitrogen admixture in the gas. In particular, the drift velocity measurements presented in this work show a reasonable agreement with calculations performed with Magboltz, although significant discrepancies are clearly visible in some cases. Our measurements have been corrected for the effect of the amplification field leaking between the cathode wires. The effect of the multiple scattering of sub-MeV electrons in xenon has been reduced to a negligible level. In the case of Xe-CO₂ mixtures, the variation of the drift velocity as a function of the N₂ admixture turns out to practically vanish at fields below 800 V/cm.

Gain measurements have been performed with mixtures with CO₂ and admixtures of N₂. A phenomenological quantification of the Penning mechanism, namely further ionisation from excited species formed in the avalanche, has been

proposed and calculated with the Magboltz 2 simulation program. The measured gain curves are only reproduced by the calculations including this mechanism. Penning transfer is somewhat inhibited by the presence of N_2 in the argon-based mixtures. In the case of the heavier xenon mixtures, the role of N_2 in this respect seems to be negligible. The results can also be found in [99].

Chapter 9

Background in the ALICE TRD based on FLUKA calculations

ALICE, the dedicated heavy-ion experiment at the CERN LHC, will study a variety of colliding systems ranging from pp and pA to light and heavy nuclei. The main focus of the experiment is to study central Pb–Pb collisions at nucleon-nucleon center-of-mass energy of 5.5 TeV which are expected to result in very high particle multiplicities and a luminosity of $10^{27} \text{ cm}^{-2}\text{s}^{-1}$.

Due to such experimental conditions a high background of thermal neutrons is expected to build up as the particles shower and get stopped in the material of the detectors, magnets, support structures and in particular in the concrete of the experimental cavern.

The Transition Radiation Detector (TRD) is located in the ALICE central barrel inside the solenoidal L3 magnet and will be used for electron identification and triggering on high p_t particles. It consists of 6 layers of Xe gas with a total volume of 27.2 m^3 in the sensitive part of the detector (see chapter 8). Some of the Xe natural isotopes have resonance peaks with very high neutron capture cross-sections (up to 50 kbarn) that lead to multi-gamma deexcitation cascades which can then produce low energy electrons through Compton scattering in the Xe gas, photo-effect and conversion to electron-positron pairs. These electrons will thus create an event uncorrelated background during the active gating time of the TRD readout chambers which is $3 \mu\text{s}$. The aim of the present study is to estimate the level of this background. The simulations were based on the FLUKA interaction

and transport Monte Carlo code as it provides the best treatment of low energy neutron transport. The energy and intensity of gammas produced by thermal neutron capture in Xenon must be known in order to simulate the background in the ALICE TRD detector. Because such information is missing from the available evaluated nuclear data files, it has been necessary to reconstruct it by comparing the few existing experimental data with a NNDC database of adopted energy levels. An algorithm based on the resulting data has been implemented in the FLUKA code to simulate the full gamma cascade in all stable Xenon isotopes. The estimation of the steady state hit rates from late neutrons in the ALICE TRD detector and the effect of the thermal neutron capture in Xenon in the radiation background are presented. In addition, neutron fluences and the energy deposition in the TRD are calculated as well as the induced radioactivity of the active gas system of ALICE TRD.

9.1 Radiation transport code (FLUKA)

The FLUKA program [100, 101] is well-established in studies of cascades induced by high-energy particles in matter. Hadronic and electromagnetic cascades can be simulated from TeV energies down to keV energies (except neutrons which can be transported down to thermal energies). Hadron inelastic interactions are described in FLUKA by three models depending on the energy. Above 4 GeV the dual parton model is used [102]. Between 2.5 GeV and 4 GeV a resonance production and decay model is employed [103], modified to take into account correlations among cascades particles and nuclear effects. Between 20 MeV and 2.5 GeV the pre-equilibrium-cascade model (PEANUT) [104] is used. All three models include evaporation and gamma deexcitation of the residual nucleus [105, 106]. Light residual nuclei are not evaporated but fragmented into a maximum of 6 bodies according to a Fermi break-up model. FLUKA has been benchmarked against experimental data over a wide energy range for both hadronic and electromagnetic showers [107, 108, 109, 110].

FLUKA is used for the radiation environment simulations of ALICE. It has a full treatment of low and high energy nuclear, hadronic and electromagnetic physics processes and provides similar accuracy for the radiation due to hadrons,

muons, electrons, photons and low energy neutrons. Some FLUKA features which are of main importance for our studies are:

- Hadron-hadron and hadron-nucleus elastic and inelastic interactions from 20 MeV up to 20 TeV including evaporation, gamma nuclear deexcitation and Fermi breakup.
- Pre-equilibrium cascade model for inelastic interactions below 1.3 GeV and for capture reactions.
- Electromagnetic and μ interactions in the range 0-100 TeV including pair production, Bremsstrahlung, multiple Coulomb scattering, magnetic field transport and delta ray production.
- Particle transport for all stable hadrons, e^\pm , muons, photons.
- Neutron multigroup transport and interactions in the range 0-20 MeV.
- Neutron capture reactions with explicit photon emission.
- Accurate and detailed ionization energy loss.
- Efficient model for multiple scattering for all charge particles based on Molière's theory.

Although the thermal neutron group of FLUKA ranges from 10^{-5} eV to 0.414 eV, the corresponding cross sections have been averaged over a Maxwellian spectrum with the most probable energy at 0.025 eV corresponding to a room temperature of 293 K. Anti-neutron transport is stopped at 50 MeV, which is dictated by the available cross-section data. The transport cut for charged hadrons was set to 10 keV. Energy cuts for electromagnetic particles are more problematic, because of the increase of computing time when the cuts are set too low. Therefore the energy thresholds for electrons and photons were set to 50 keV and 30 keV, respectively.

9.1.1 Radiation units used in FLUKA

In radiation background calculations, the rates of particles in a given detector region are quantified in terms of *flux*, or *current*. These two quantities have the dimensions of number/unit-time/unit-area, but they do not have the same meaning. *Flux* counts the rate of arrivals per unit area independent of the particle direction and its real physical meaning is that of path density, whereas *current* counts the rate crossing through a given plane, referred to area elements in the surface of the plane.

The importance of flux is that if one considers lengths in mean free paths for a given reaction, then the path density is just equal to the reaction density. *To measure lengths in mean free paths* means to multiply the lengths in cm by the cross section and by the atom density. Thus, every time we want to score a quantity which is proportional to any effect which has a cross section, or a mean free path, we must score flux. Current is meaningful only for counting particles independent of any effect they may produce in matter.

In FLUKA *flux* is defined either as the track-length of a particle per unit of volume, or as the number of particles hitting a sphere of unit cross-section per unit time and its unit can be expressed as ($\text{cm}^{-2}\text{s}^{-1}$). *Fluence* is the time integral of flux expressed in units of (cm^{-2}). Only in the special case of normal incidence on a flat surface the flux is equal to the number of particles crossing a unit surface. For particles arriving at an angle to a flat surface the flux is the number of particles crossing a unit surface per unit of time weighted by $(1/\cos\theta)$, where θ is the angle with respect to the normal of the surface [111].

A *star* is a hadronic inelastic interaction (spallation reaction) at an energy higher than a user-defined threshold (or by default higher than the transport threshold of the interacting particle). Star scoring (traditionally used in most high-energy shielding codes) can therefore be considered as a form of crude collision estimator: multiplication of the star density by the asymptotic value of the inelastic nuclear interaction length gives the fluence of hadrons having energy higher than the current threshold.

Selecting star scoring is meaningful for hadrons, photons and muons (if their energy is sufficiently high). Any other particle will not produce any star. More-

over, in FLUKA stars do not include spallations due to annihilating particles. The results are expressed in stars/cm³/primary particle.

The scoring by regions enables the calculation of the *energy deposition* in different detectors represented by different regions. Energy deposition is expressed in GeV/cm³/primary particle. To obtain *doses* (in Gy per unit primary particle), the results must be multiplied by $(10^{12} \times e / \rho \times V)$, where ρ is the material density in g/cm³, e the electron charge in C and V the volume of the region in cm³. The fluence of charged particles and the absorbed dose, are correlated for a given particle type and energy in a given medium. Assume a minimum ionizing particle passing through an object and interacting only by dE/dX energy loss due to ionization. The damage will depend on accumulated track-length, even in the case of very thin detectors, and the damage scales with the flux, since the accumulated track-length does not depend on orientation. For charged particles, track-length is proportional to the energy deposited ($E_{\text{dep}} = L \times S$, where L is the tracklength and $S = dE/dX$ is the stopping power).

To sum up, star density by producing particle and region as well as energy deposition by region, total or from electrons/photons only can be scored. Moreover, fluence and current scoring as a function of energy can be done via boundary-crossing, collision and track-length estimators coincident with regions or region boundaries.

9.2 Implementation of Xenon capture gammas in FLUKA

The ALICE Transition Radiation Detector (TRD) [112, 113] will be a 6-layer barrel detector surrounding the interaction point at radial distances from 2.9 to 3.7 meters. Each layer will include radiator and a drift chamber filled with a gas mixture containing 85% of Xenon.

The TRD has been designed to provide a separation of pions and electrons with momenta larger than 0.5 GeV/c, based on Transition Radiation (TR) photons which are produced by electrons when traversing the radiator. Such photons, with typical energies between 4 and 30 keV, have an absorption length of the

order of 1 cm in Xenon at STP.

Nominal rejection factors for pions have also been measured experimentally [114] in test beams with prototype and real size detectors [115, 116, 117], but the actual separation power will depend in a complex way on the intensity, composition and time structure of the radiation background which will be present in the real LHC environment.

To predict the characteristics of such background, accurate Monte Carlo simulations are needed, taking into account the particles issued from the initial collision as well as their secondaries, and the interaction of the latter not only with the different parts of the experiment but also with the accelerator structure and with the concrete walls of the tunnel.

Some of the secondaries are neutrons which become thermalized by repeated scattering in the surrounding structures and after a relatively long time (typically several milliseconds) are eventually captured by a nucleus. The resulting nucleus is left in an excited state, generally about 7 or 8 MeV above the ground level, and de-excites by releasing its excitation energy as a cascade of gamma rays. These interact in turn by releasing electrons and producing a signal uncorrelated with the initial particles. Such noise, which tends to hide the signal of the particles issued directly from the collision, needs to be evaluated by detailed Monte Carlo calculations.

9.2.1 Neutron transport and (n,γ) reactions in FLUKA

In the FLUKA Monte Carlo program [100], the transport of neutrons with energies lower than 20 MeV is performed by a multigroup algorithm. In the standard FLUKA cross-section library [118], the energy range up to 20 MeV is divided into 72 energy groups of approximately equal logarithmic width, one of which is thermal. The angular probabilities for inelastic scattering are obtained by a discretization of a P5 Legendre polynomial expansion of the actual scattering distribution which preserves its first 6 moments.

In general, gamma generation (but not transport) is also treated in the frame of a multigroup scheme. A so-called “downscattering matrix” provides the probability, for a neutron in a given energy group, to generate a photon in each of 22

gamma energy groups, covering the range 10 keV to 20 MeV. With the exception of a few important gamma lines, such as the 2.2 MeV transition of Deuterium, the actual energy of the generated photon is sampled randomly in the energy interval corresponding to its gamma group. Note that the gamma generation matrix does not include only capture gammas, but also gammas produced in other inelastic reactions such as (n,n') .

The gamma generation probabilities, as well as the neutron total and differential cross sections, kerma factors and information on production of residual nuclei, are derived from Evaluated Nuclear Data Files, distributed by specialized Centres such as the NEA Data Bank [119], RSICC [120] and the IAEA [121], by processing them with an appropriate code [122]. Since several evaluated cross section sets are available, with variable degrees of completeness and reliability, an effort is constantly being made to include in the FLUKA library the best data available at a particular time. Presently, the library includes about 120 different materials (elements or isotopes, in some cases with the possible choice of different molecular bindings, temperatures or degrees of self-shielding). However, while transport cross sections are available for all materials of the library, for a few of them it has not been possible so far to find evaluated data concerning some of the complementary information (gamma production, kerma factors or residual nuclei).

As stressed above, a proper simulation of capture gammas in Xenon is an essential ingredient of any background prediction for the ALICE TRD, but unfortunately gamma generation information is missing in the Xenon entry of the FLUKA neutron cross section library, since no corresponding evaluated data have been found. However, much of the basic information is available in the form of recommended level energies, published regularly on the journal Nuclear Data Sheets and available also on-line [123]. These recommended levels have not been identified necessarily only in (n,γ) reactions, but have been derived also from experiments on beta decay, heavy ion reactions, etc. And indeed, many of them don't play any role in neutron capture because of quantum selection rules, but in most cases it is possible to select the relevant ones by a cross check with Xenon capture gamma energies reported by experimental papers and by following all the possible paths of the gamma cascade from the capture level (easily calculated by

an energy-mass balance) down to the ground state. Combining all this material together, and making some reasonable physical assumption about the information which is still missing, it has been possible to write a FLUKA subroutine providing an acceptable description of $\text{Xe}(n,\gamma)$ reactions.

A similar work was done some time ago to implement in FLUKA capture gammas from another important nuclide for which evaluated data were missing, ^{113}Cd . However, the approach has not been identical in the two cases. First, in the case of Cadmium only the most important isotope was considered, while in the case of Xenon all 9 stable isotopes have been taken into account. In addition, the type of available experimental data was different for the two elements: for Cadmium, in addition to level energies and relative intensities, gamma energies and absolute gamma ray intensities (probabilities per neutron capture) were available. However, since the existence of unobserved transitions was evident from the intensity balance, a simple deexcitation model has been applied to complete the decay scheme.

9.2.2 Basic nuclear data for Xenon

Element Xenon (atomic number 54) has 9 stable isotopes, with mass number 124, 126, 128, 129, 130, 131, 132, 134, 136 (^{124}Xe and ^{136}Xe are actually unstable, but with an extremely long half-life). Their abundances [124] and their nuclear masses [125] are reported in Table 9.1. In the same Table are reported also the atomic masses¹ of the nuclei formed by neutron capture in those nuclei.

The respective Q-values for (n,γ) reaction, as given by the formula:

$$Q = u \left({}_{54}^A M + M_n - {}_{54}^{A+1} M \right)$$

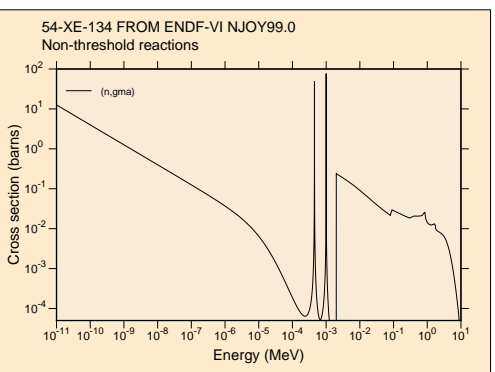
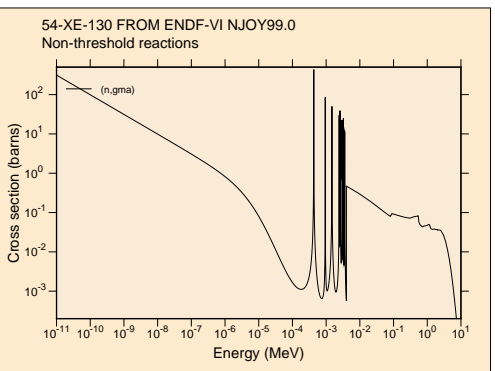
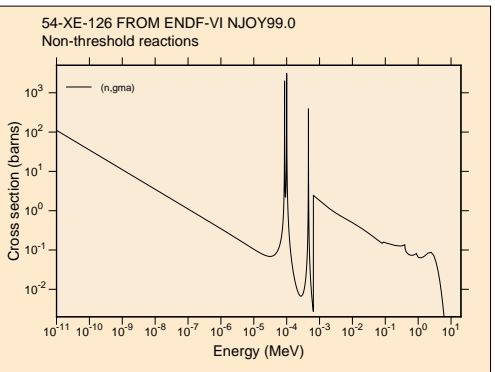
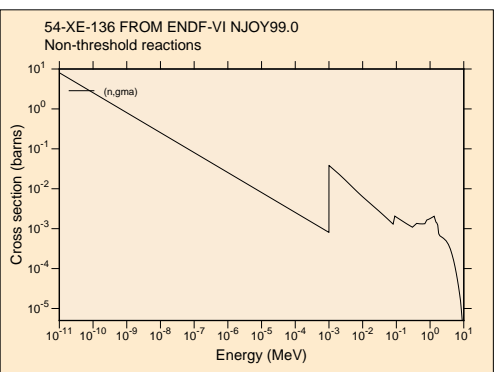
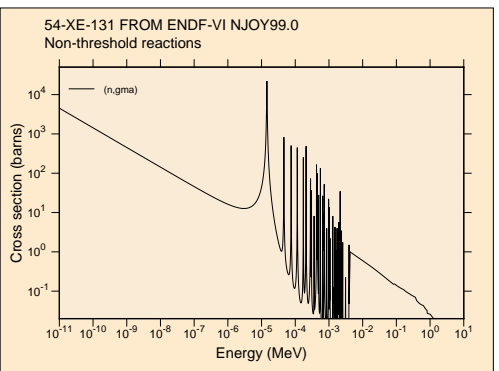
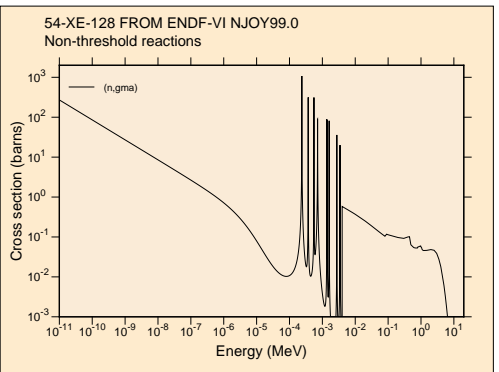
where u is the atomic mass unit (931.494013 MeV), and M_n is the neutron mass (939.56533 MeV). Plots of (n,γ) cross sections as a function of energy for the 9 natural isotopes of Xenon, derived from ENDF/B-VI files [126] are shown in Fig. 9.1.

¹The evaluated data refer to *atomic* masses, but internally FLUKA uses *nuclear* masses obtained by the latter by subtracting the electron masses and adding the electron binding energies

9.2. IMPLEMENTATION OF XENON CAPTURE GAMMAS IN FLUKA105

Xenon isotope	A ${}_{54}^A M$ (amu)	$A+1$ ${}_{54}^{A+1} M$ (amu)	Abundance %
${}^{124}\text{Xe}$	123.9058958	124.9063982	0.09
${}^{126}\text{Xe}$	125.9042689	126.9051796	0.09
${}^{128}\text{Xe}$	127.9035304	128.9047795	1.92
${}^{129}\text{Xe}$	128.9047795	129.9035079	26.44
${}^{130}\text{Xe}$	129.9035079	130.9050819	4.08
${}^{131}\text{Xe}$	130.9050819	131.9041545	21.18
${}^{132}\text{Xe}$	131.9041545	132.9059057	26.89
${}^{134}\text{Xe}$	133.9053945	134.907207	10.44
${}^{136}\text{Xe}$	135.907220	136.911563	8.87

Table 9.1: Masses and abundances of naturally occurring Xenon isotopes, and masses of the nuclei formed by neutron capture



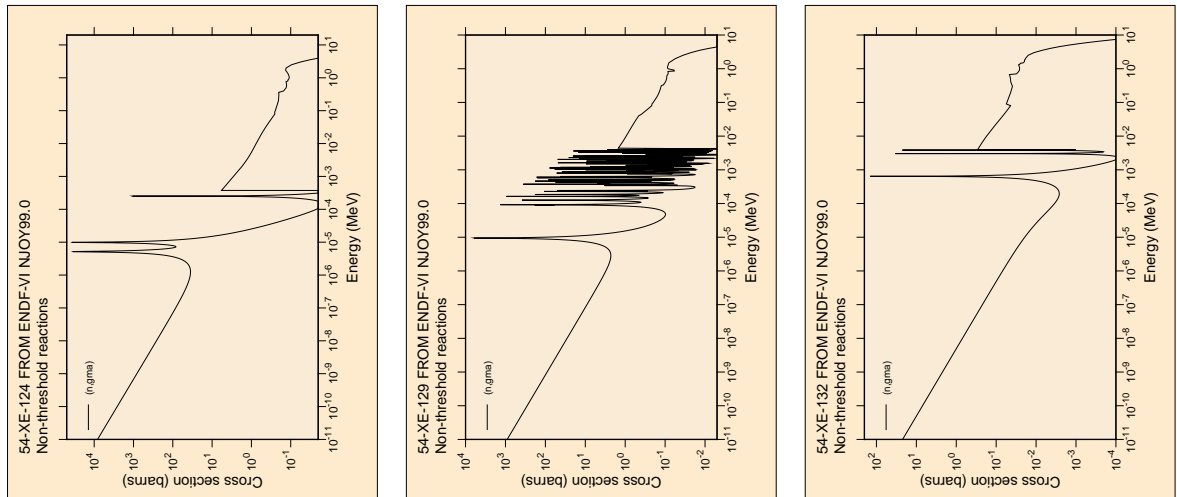


Figure 9.1: ENDF/B-VI (n, γ) cross sections of Xenon isotopes

9.2.3 Available information on energy levels

Measured and recommended values for the energy levels of all known nuclides are reported monthly on the journal Nuclear Data Sheets [127]. The same data and decay schemes can be retrieved on-line from the Evaluated Nuclear Structure Data File (ENSDF) [128]. The NuDat program [123] provided by NNDC (National Nuclear Data Center at the Brookhaven National Laboratory), allows to extract the recommended values in the form of tables which can be easily read and processed by a user program. For each level, recommended gamma energies, intensities and multiplicities are listed, as well as the level half-life and the spin and parity, when known.

These recommended levels and gamma transitions, which have been derived from a variety of nuclear reaction and decay experiments, do not include virtual

excitation levels populated by neutron capture. The energy of latter is easily calculated anyway by adding the Q-value (see Table 9.1) and the kinetic energy of the captured neutron, but the energies and intensities of gammas emitted from the virtual levels can be obtained only from published experiments on neutron capture (all rather old in the case of Xenon). Such data are reported on Nuclear Data Sheets, but exactly as they were published, without any evaluation of the gamma energies to make them consistent with the adopted energies of all other levels. Also, only measurements made on single isotopes are considered. Such experimental data are available for ^{130}Xe [129, 130], ^{132}Xe [129, 131] and ^{137}Xe [132, 133] but not for the other six Xenon isotopes.

With some difficulty, additional information can be extracted also from experimental data obtained with Xenon of natural isotopic composition. The popular “Lone-Catalog” [134] is a compilation of energies and relative intensities of capture gamma rays for all elements up to $Z = 83$. For Xenon, 161 gamma lines are reported. However, a comparison with presently recommended values and with the available single-isotope data mentioned above shows that the compilation cannot be considered as very reliable, despite the fact that it is still proposed as a reference by NNDC [135] (for a discussion of the quality of these data see [136]).

A much better source for Xenon capture gammas is a paper by Hamada *et al.* [137], where 273 gamma lines are reported. The authors have assigned some of these lines to ^{130}Xe and ^{132}Xe , but a systematic comparison with differences between adopted levels has allowed to assign practically each gamma line to one of the stable isotopes of Xenon. Several of the gamma energies reported in [137] have also been found to correspond, within small uncertainties, to transitions from the virtual level of one of the Xenon isotopes to one of the corresponding adopted levels.

9.2.4 Implementation in FLUKA

As can be understood from the previous survey of available data, it is impossible at the present time to establish a complete database of capture gamma lines for Xenon. However, a large number of gamma lines (820) have been identified, corresponding to transitions between 335 levels. More details are given in Table 9.2.

The implementation in FLUKA has been based on the relative branching ratios within each level, which are well established, rather than on the poorly known absolute intensities (number of gammas per capture) or even than on relative intensities over all levels. Gamma lines from a given level for which no relative intensity was reported were assumed to be equally distributed among the known branchings; when the intensity was expressed for instance as “< 80”, one-half of that value was assumed. In a few cases, when different transitions from the same virtual level were reported by two sources, the values were merged after a re-normalisation of intensities based on all those lines which were common to both.

The resulting database does not include explicitly gamma energies, but only level energies and, for each level, the possible transitions to lower levels with the respective cumulative probabilities. In this way, each gamma energy is obtained by difference between its starting and ending level, and exactly the same total gamma energy is emitted for any possible path of the gamma cascade from the virtual to the ground level.

Energy conservation on a more global level is ensured by calculating the recoil of the nucleus in the laboratory frame, based on an accurate balance of all masses concerned. The photon emission is assumed to be isotropic.

Of course, several approximations have been necessary. While the energy of the virtual level is calculated correctly taking into account the kinetic energy of the captured neutron, it has been assumed that the possible transitions and their relative intensities do not depend on the neutron energy. This assumption is unlikely to be valid at energies at which the reaction proceeds predominantly through p-wave capture, but a rigorous analysis to identify these energies has not been made. First of all, there is no sufficient experimental or theoretical information which would allow to establish different transitions and intensities. On the contrary, some of the published gamma transitions we have used were not obtained at thermal energies but at some resonance energy [130, 131], because this is the simplest way to study transitions in an individual isotope. But even if such information would exist, its implementation in FLUKA should take into account a different situation for each of the 9 Xenon isotopes, making the database and the dedicated routine exceedingly complex. Also, it could be possible to avoid

9.2. IMPLEMENTATION OF XENON CAPTURE GAMMAS IN FLUKA109

Xenon isotope	Number of levels		Number of gammas			
	adopted in NuDat	used in FLUKA	adopted in NuDat	used in FLUKA, from:		
				lower levels	virtual level	total
^{124}Xe	234	80	633	175	24	199
^{126}Xe	108	46	233	81	12	93
^{128}Xe	58	28	109	45	9	54
^{129}Xe	103	72	207	144	45	189
^{130}Xe	43	19	66	24	6	30
^{131}Xe	75	30	200	87	18	105
^{132}Xe	29	13	56	24	4	28
^{134}Xe	29	15	86	38	3	41
^{136}Xe	164	32	213	53	28	81

Table 9.2: Number of Xenon energy levels and gammas: adopted in NuDat and implemented in FLUKA

the problem by implementing gamma production only for thermal neutrons and epithermals with energies lower than any resonance, but it has been judged better to produce some gammas with the wrong energy or probability rather than producing none at all: at least, the total excitation energy will be correctly accounted for as gamma radiation and the overall energetic balance will be satisfied.

On the other hand, the implementation would be too grossly incorrect — or too complicated to do correctly — if it would extend also above the threshold for inelastic neutron scattering. Therefore, an upper limit of 39 keV (isotope-independent for the sake of simplicity) has been set for the energy of any neutron which can be captured in with gamma emission in Xenon. Table 9.3 shows the different thresholds for (n,n') reaction in Xenon isotopes, obtained from the ENDF/B-VI evaluated file [126].

It is also possible, as it was found in the case of Cadmium, that not all transitions from the virtual level have been identified. However, too little information is available for Xenon concerning absolute gamma emission probabilities. Therefore, no attempt has been made at filling gaps of unknown size.

Xenon isotope	Q (MeV)	nuclide ${}^A_{54}\text{Xe}$	Q (MeV)	nuclide ${}^A_{54}\text{Xe}$	Q (MeV)
${}^{124}\text{Xe}$	-0.357	${}^{129}\text{Xe}$	-0.040	${}^{132}\text{Xe}$	-0.668
${}^{126}\text{Xe}$	-0.389	${}^{130}\text{Xe}$	-0.536	${}^{134}\text{Xe}$	-0.847
${}^{128}\text{Xe}$	-0.443	${}^{131}\text{Xe}$	-0.080	${}^{136}\text{Xe}$	-1.313

Table 9.3: Q-values for neutron inelastic scattering in the naturally occurring isotopes of Xenon

9.2.5 Discussion

Despite the approximations which have been described above, the new FLUKA description of capture gammas from neutron capture in Xenon should give better results than the default multigroup description used for most FLUKA materials. The energy of each photon is determined as the exact difference between two energy levels, instead of being sampled randomly in a certain energy interval; but — even more important — the correlations between photons emitted by the same excited nucleus will be reproduced correctly in most cases. This should be of a particular interest for the simulation of the high-energy physics detector which has triggered this work.

Extensions of the present approach to other nuclides are possible, provided that good data on the transitions from the virtual levels are available. Otherwise, it will be necessary to derive them from a physical model, similar to what has been done for ${}^{113}\text{Cd}$. However, if the number of nuclides considered should increase beyond a certain limit, it could be preferable in future to read the level data from an external data file, rather than having them hard-wired in a routine specific for each element.

By following each possible sequence of level transitions and compounding the product of their respective probabilities with the abundance and with the relative capture cross section of the isotope concerned, it is possible to calculate an absolute intensity for each gamma produced. The 689 gamma energies having an intensity larger than 10^{-3} per 100 neutron captures are reported in an ALICE Internal Note [145] (see appendix B). Here the 28 most intense ones are shown

9.2. IMPLEMENTATION OF XENON CAPTURE GAMMAS IN FLUKA111

in Table 9.4.

Two different tests were done. In one test, many neutron captures in a quasi-infinite Xenon volume were simulated, and the length of the photon tracks versus the photon energy was scored. All the photons produced travelled some distance before being captured or escaping. So, for each capture we get all the energies of the transition tree. In addition, we get also tracks of photons which had been scattered and therefore had not the initial energy anymore. In the second test, we did not do any simulation, but simply traversed each branch of the tree in a separate program. There was no transport, but just a check of all possible transition combinations.

Fig. 9.2 shows a gamma line spectrum obtained in a standalone test of the new FLUKA routine which generates capture gammas in Xenon. The input neutrons energies were randomly sampled from a Maxwellian distribution in the energy range 10^{-5} to 0.4 eV, corresponding to the thermal neutron group of FLUKA and the target nucleus was sampled according both to its abundance and to its thermal neutron capture cross section. As it can be expected from Table 9.4, the most frequent lines belong to ^{132}Xe (667.72, 772.60, 1317.93 and 6466.07 keV, the latter corresponding to a transition from the capture level). The 536.09 keV line is from ^{130}Xe .

A test of the new routine has been done also with a FLUKA run in an idealized geometry: an isotropic 0.025 eV neutron point source in the middle of an “infinite” cube of Xenon. Fig. 9.3 shows the calculated track length of photons as a function of photon energy. Comparing this spectrum with that of Fig. 9.2, the following differences can be noticed:

- the presence of a high 511 keV peak, due to positron annihilation
- a progressive decrease of the gamma line intensity with decreasing energy, due to increasing absorption by photoelectric effect
- a broad Compton background, hiding most of the lower energy lines

Real situations should be more complex, of course, since neutron capture in surrounding structural materials would provide additional gammas of different energies and would even be probably dominant. But, due to the high

energy of most capture gammas and to their ability to create electron pairs, the largest contribution can still be expected to be that of the annihilation peak.

Appendix: Preparation of FLUKA input

To activate the new scheme of capture gammas in Xenon, two things are required. Command LOW-NEUT must be issued with `WHAT(6) = 1.0` (or 11.0 if a special fission biasing is also requested), and material XENON must be defined as a `COMPOUND`, consisting of its 9 natural isotopes with the respective abundances (see Table 9.1). Single-isotope materials are defined by setting `WHAT(6) =` the mass number of the isotope in the corresponding `MATERIAL` command.

Example (note the compulsory names of the 9 isotopes as they are now defined in the neutron cross section library):

```
*...+...1...+...2...+...3...+...4...+...5...+...6...+...7...+...
LOW-NEUT      72.0    22.0  0.0196    0.0    1.0    1.
MATERIAL      54.0   123.9 5.4854E-3  26.0    0.0   124. 124-XE
MATERIAL      54.0   125.9 5.4854E-3  27.0    0.0   126. 126-XE
MATERIAL      54.0   127.9 5.4854E-3  28.0    0.0   128. 128-XE
MATERIAL      54.0   128.9 5.4854E-3  29.0    0.0   129. 129-XE
MATERIAL      54.0   129.9 5.4854E-3  30.0    0.0   130. 130-XE
MATERIAL      54.0   130.9 5.4854E-3  31.0    0.0   131. 131-XE
MATERIAL      54.0   131.9 5.4854E-3  32.0    0.0   132. 132-XE
MATERIAL      54.0   133.9 5.4854E-3  33.0    0.0   134. 134-XE
MATERIAL      54.0   135.9 5.4854E-3  34.0    0.0   136. 136-XE
*
MATERIAL      0.0     0.0 5.4854E-3  35.0    0.0    0. XENON
COMPOUND     -0.09   26.0  -0.09   27.0   -1.92   28. XENON
COMPOUND    -26.44   29.0  -4.08   30.0  -21.18   31. XENON
COMPOUND    -26.89   32.0 -10.44   33.0   -8.87   34. XENON
```

9.2. IMPLEMENTATION OF XENON CAPTURE GAMMAS IN FLUKA113

Xenon isotope	Gamma energy (keV)	From level (keV)	To level (keV)	I_γ per 100 captures
^{132}Xe	667.72	667.72	0.0	64.73
^{132}Xe	6466.1	8935.2	2469.1	24.07
^{132}Xe	772.61	1440.3	667.72	22.55
^{130}Xe	536.09	536.09	0.0	16.60
^{132}Xe	1317.9	1985.7	667.72	15.88
^{132}Xe	6379.8	8935.2	2555.4	10.66
^{130}Xe	668.52	1204.6	536.09	10.25
^{132}Xe	483.46	2469.1	1985.7	9.824
^{132}Xe	600.03	2040.4	1440.3	8.355
^{132}Xe	5754.4	8935.2	3180.8	7.847
^{132}Xe	569.75	2555.4	1985.7	7.196
^{132}Xe	1028.8	2469.1	1440.3	6.778
^{132}Xe	1887.7	2555.4	667.72	6.404
^{125}Xe	111.78	111.78	0.0	6.344
^{132}Xe	1140.4	3180.8	2040.4	6.278
^{130}Xe	739.48	1944.1	1204.6	5.859
^{132}Xe	5142.9	8935.2	3792.3	5.783
^{132}Xe	1801.4	2469.1	667.72	5.501
^{130}Xe	752.79	2696.9	1944.1	5.344
^{130}Xe	275.45	2972.3	2696.9	5.225
^{130}Xe	720.84	3693.2	2972.3	4.921
^{125}Xe	140.82	252.60	111.78	4.608
^{132}Xe	630.20	1297.9	667.72	4.384
^{132}Xe	8267.5	8935.2	667.72	4.323
^{132}Xe	5235.7	8935.2	3699.5	4.186
^{130}Xe	854.99	2059.6	1204.6	3.992
^{125}Xe	57.940	310.54	252.60	3.917
^{130}Xe	315.60	2375.2	2059.6	3.666

Table 9.4: Number of gammas per 100 thermal neutron captures in ^{nat}Xe

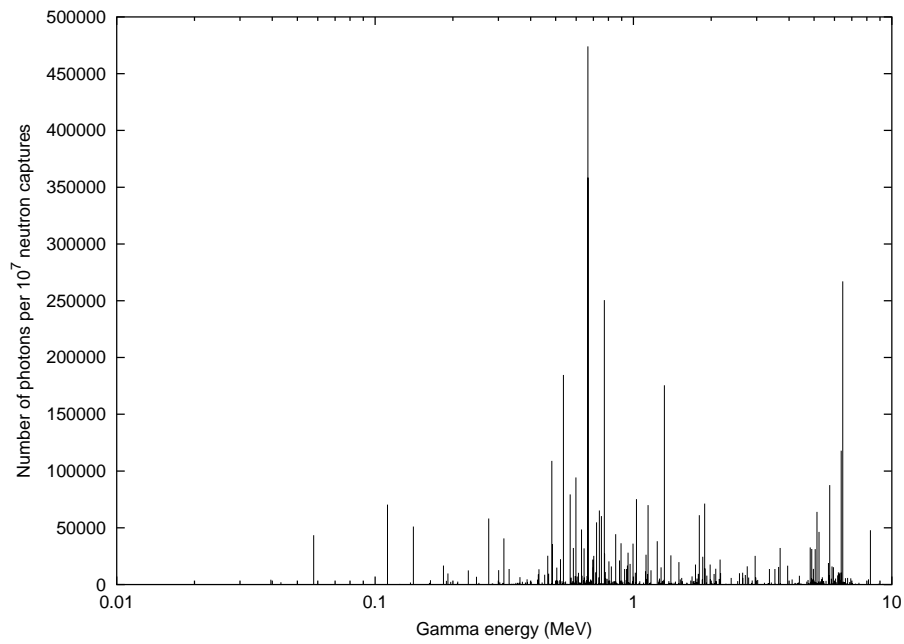


Figure 9.2: Gamma lines generated in 10^7 neutron captures in Xenon

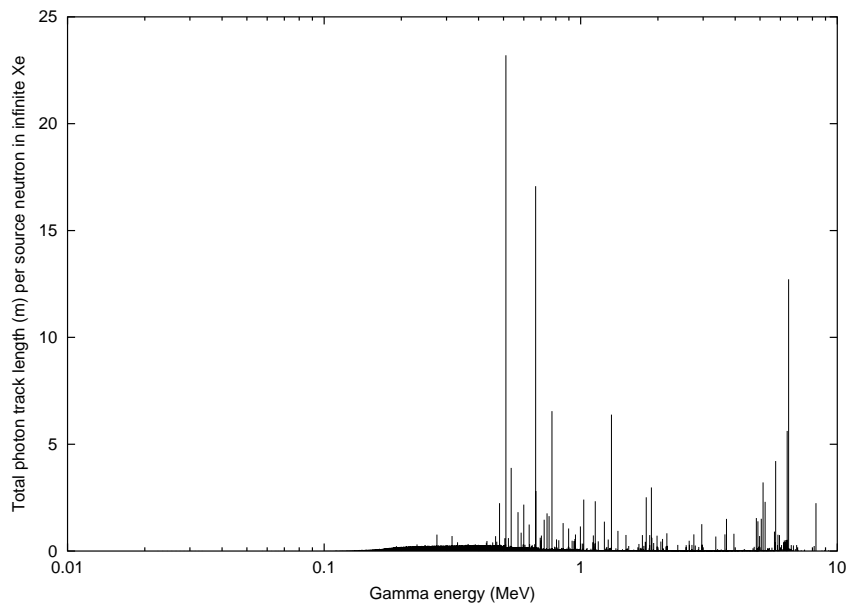


Figure 9.3: Photon track length spectrum calculated by FLUKA for a thermal neutron source in an infinite Xenon volume

9.3 Background from thermal neutrons

9.3.1 Description of the detector geometry and material

FLUKA uses the combinatorial geometry in order to describe general three dimensional material configurations by considering unions, differences and intersections of simple bodies such as spheres, boxes, cylinders, etc. A flexible tool, the ALIFE [139] editor and parser, was developed in ALICE, to facilitate the preparation of the FLUKA input cards which are used to define the geometry, material, as well as tracking and scoring options.

The ALICE experimental area as simulated in FLUKA is shown in Figs. 9.4 and 9.5. All lines represent boundaries between different materials as used in the calculations. The geometry [140] is described in a right handed orthogonal system with origin at the ALICE interaction point, the x -axis vertical, the y -axis pointing towards the centre of the LHC ring and the z -axis along the beam direction.

About 3200 volumes and 1500 regions are needed to describe the ALICE detector and experimental area including the cavern, tunnels, vertical shafts, shielding, inner triplet and separation dipoles, surrounding hall, beam elements and the ALICE detectors racks. Since the aim is to study the background all detectors were described with the appropriate accuracy and correct amount of material on average; however not in the detail required for tracking performance studies and as implemented in AliRoot [141], the Geant [142] based simulation of the experiment. Particle back-scattering in the concrete walls of the caverns and shafts is taken into account by approximating the walls by a 30 cm layer of concrete. Regions behind this layer are treated as ‘black-holes’, i.e. as regions that absorb all particles that enter them. Magnetic fields were taken into account in five different parts of the geometrical setup: the L3 magnet, the muon spectrometer, the dipole magnet compensating the field in the muon spectrometer, the inner quadrupole triplet and separation/recombination dipole magnet D1.

The TRD layout as described in FLUKA is shown in Fig. 9.6. It is approximated by 6 sets of concentric cylindrical layers each one of them consisting of 9 layers of different materials with thickness summarized in Table 9.5 in accordance with the description of the detector in the TRD TDR [113].

Table 9.5: The FLUKA materials in the TRD and their thickness.

FLUKA materials in the TRD	Thickness (cm)
Air	3.923
Polyethylene (Rohacell)	4.8
Mylar	0.005
Xenon	3.5
Copper	0.001
Read out (G10)	0.06
Signal lines (Copper)	0.005
Cooling Al (Aluminum)	0.02
Cooling Water	0.02

9.3.2 Primary event generation and scoring

The radiation environment for this study is based on minimum bias events. The parametrized HIJING event generator [143] was used to generate pions and kaons according to parametrized pseudo-rapidity η and p_t distributions.

The produced events with average multiplicity of 80 000 primary particles were used as input for FLUKA and transported through the material of the experiment and experimental area.

Boundary crossing scoring was used to estimate the number of particles that passed through the 6 Xe layers or were created there by using a user-defined boundary crossing fluence or current estimator for each of the 6 different Xe layers. All particles entering the scoring region are ‘tagged’ to avoid double counting and the particles which leave the scoring volume are ‘untagged’ so they can be detected again. In the case of electrons or

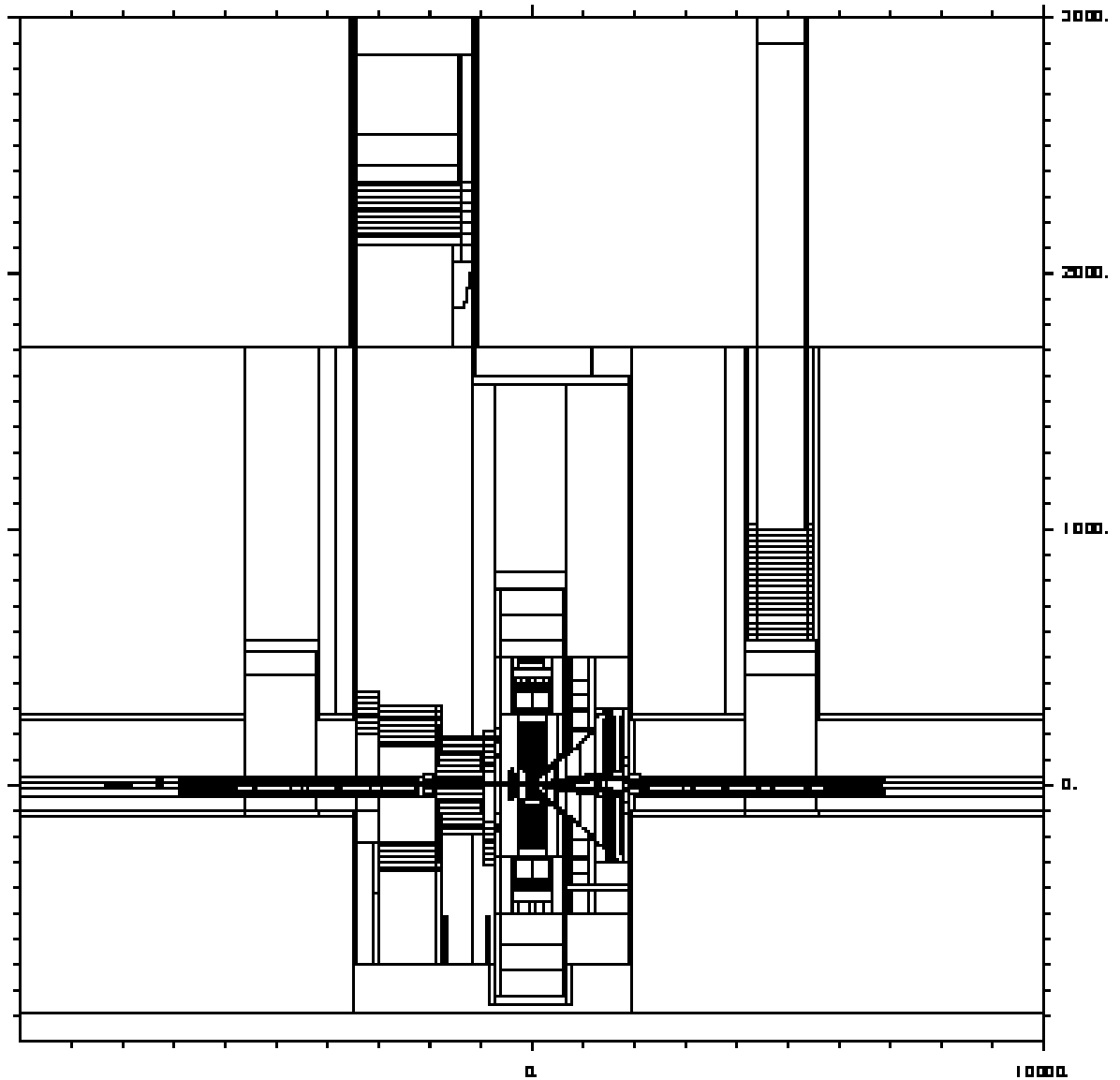


Figure 9.4: The geometry of the ALICE experimental area as implemented in FLUKA (vertical longitudinal section through the main experimental cavern UX25, the counting room shaft PX24 and the shaft PGC2).

positrons from gamma reaction it is the gamma that is actually tagged and the gamma production vertex is scored.

As low energy electrons can interact many times in the gas layer and pro-

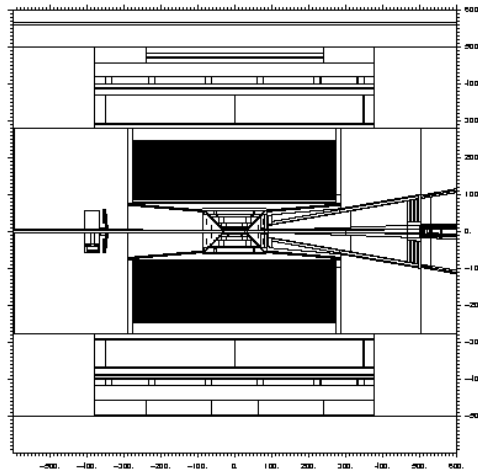


Figure 9.5: The geometry of the central detector as implemented in FLUKA (vertical cross-section).

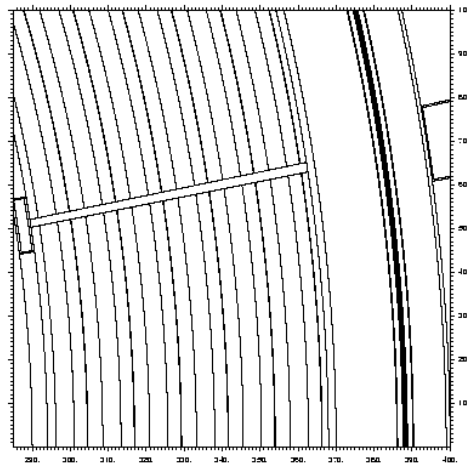


Figure 9.6: The geometry of the TRD detector as implemented in FLUKA.

duce many hits, it was necessary to optimise the electron step length by scoring the energy deposited in many steps along its trajectory. The boundary crossing estimator in conjunction with the energy deposition in steps is a sufficient way to estimate the number of electron hits and the charge deposition from the number of their tracking steps in a given detector.

9.3.3 Particle fluxes and energy deposition in the TRD, with and without neutron capture in Xenon

The way used to calculate particle fluxes in the TRD is via a special tool of FLUKA the track-length estimator. Defining 6 such estimators, each of them pointing on one Xe layer region and taking the average from them during one FLUKA event (a minimum bias event), we calculate the total track-length of electrons, photons and neutrons, normalized per source particle. The results are summarized in Table 9.6 with and without neutron capture in Xenon respectively.

Table 9.6: Total track-length of electrons, photons and neutrons, normalized per source particle with and without neutron capture in Xenon (2nd and 3rd column respectively).

Particles	Track-length (cm/primary)	
electrons	1.74±0.3	1.4±0.15
photons	57.23±2.8	47.98±2.12
neutrons	148.07±9.4	146.05±9.1

The total track-length of electrons and photons is higher **24%** and **19%** respectively taking into account the neutron capture in Xenon. The track-length is more meaningful than the number of particles, because any signal, or any damage, is proportional to the energy deposited, or to the number of collisions which are all proportional to the track-length. Dividing the total track-length with the volume of the scoring region we obtain the total response or *cumulative fluence* expressed as (particles/cm²/primary).

The results of the FLUKA track-length estimator are always given as differential distributions of fluence in energy (cm⁻² GeV⁻¹ per incident primary unit weight). In figures displaying differential fluence versus energy over a large range of energy, the abscissa is often the logarithm of energy [144]. In making the coordinate transformation from linear energy and particle-differential fluence distribution $d\Phi/dE$ to logarithmic energy, it is desirable

to preserve the fact that relative areas in different energy regions represent relative fluences. This can easily be accomplished by multiplying the conventional particle-differential fluence distribution $d\Phi/dE$ by the energy because $d\Phi/d(\log E) = d\Phi/(dE/E) = E d\Phi/dE$.

Figures 9.7, 9.8 and 9.9 are designed to allow visual integration of fluence having the areas under the curves proportional to the fluence (lethargy spectra) and were taken with and without neutron capture in Xenon in one Xenon layer for electrons, photons and neutrons respectively.

Comparing the photon spectra (Fig. 9.8) by activating or not the neutron capture in Xenon, it can be noticed the presence of a much higher 511 keV peak (due to positron annihilation) as well as the most frequent gammas in Xenon from the isotope ^{132}Xe . Concerning the 2.2 MeV peak from the neutron capture in Hydrogen and the 7.9 MeV in Copper, both peaks are there and identical, whether the neutron capture gammas in Xenon are activated or not. Due to the high energy of most capture gammas and to their ability to create electron pairs, the largest contribution is expected to be that of the annihilation peak.

The lethargy spectrum of electrons (Fig. 9.7) indicates that when the neutron capture gammas in Xenon are activated, electrons with energy from 50 keV to 500 keV have greater track-length and energy deposition.

The energy deposition in one Xenon layer, total or from electrons, positrons and photons (all together), by activating the neutron capture in Xenon is:

→ Total energy deposition : $\sim (4.32 \pm 0.31) \times 10^{-5}$ GeV per source particle.

→ Energy deposition from electrons, positrons and photons : $\sim (3.05 \pm 0.22) \times 10^{-5}$ GeV per source particle.

Without including in the simulation the neutron capture in Xenon is:

→ Total energy deposition : $\sim (3.98 \pm 0.3) \times 10^{-5}$ GeV per source particle.

→ Energy deposition from electrons, positrons and photons : $\sim (2.7 \pm 0.13) \times 10^{-5}$ GeV per source particle.

Therefore, all the additional energy deposition that is expected from the neutron capture in Xenon is in fact EM energy about 10 % more.

Due to the high neutron flux in the TRD detector it is important to be aware of the cumulative fluence of the dominating thermal neutrons. Scoring in the six Xenon layers during one event and taking the average value it can be noticed:

→ Total neutron fluence per primary in the TRD is : $\sim (27 \pm 3) \times 10^{-6}$ neutrons/cm².

→ Thermal neutron fluence per primary in the TRD is : $\sim (8 \pm 1) \times 10^{-6}$ neutrons/cm².

To scale up to a ten-year run period we multiply the aforementioned results with a factor of 3.2×10^{15} (80000 primaries \times 8 KHz / $5 \times 2.5 \times 10^6$ sec/year \times 10 years). The following Table 9.7 shows the resulting dose in a Xe layer accumulated during ten years of operation as well as the energy deposition, the neutron and thermal neutron fluence.

Table 9.7: Neutron fluences, energy depositions and absorbed doses in one Xenon layer of the TRD per 10 ALICE years.

Neutron Fluence [cm ⁻²]	$(8.64 \pm 0.96) \times 10^{10}$
Thermal neutron Fluence [cm ⁻²]	$(2.56 \pm 0.32) \times 10^{10}$
Total Edep [GeV]	$(1.38 \pm 0.10) \times 10^{11}$
Edep from e [±] , γ [GeV]	$(0.98 \pm 0.07) \times 10^{11}$
Total Dose [Gy]	$(7.45 \pm 0.54) \times 10^{-1}$
Dose from e [±] , γ [Gy]	$(5.26 \pm 0.38) \times 10^{-1}$

9.3.4 Evaluation of the steady state background hit rate in the TRD

The FLUKA simulations indicate that, for the geometry and materials present in the experiment, thermalization time (the time for the neutron kinetic energy to reach 1/40 eV) is of the order of a few μs .

Neutrons are slowed down inside the detector module and surrounding material, become thermalized and eventually some of them get captured by a nucleus after several μs . Therefore, the start of the neutron capture according to the scope of this study is set 10 μs after the collision. The energy spectra of the early and the delayed neutrons as well as their age vs energy distribution are shown in Figs. 9.10 and 9.11 respectively.

The secondaries inside the TRD after 10 μs are only neutrons, photons, positrons and electrons. Their time spectra are shown in Fig. 9.12. The dashed lines (red curves) have been obtained by activating the neutron capture in Xenon and the solid (blue) without.

By integrating the distributions of the delayed particles for each FLUKA event it can be estimated that due to neutron capture in Xenon we will have:

- $(30\pm 6)\%$ more photons
- $(26\pm 7)\%$ more electrons
- $(19\pm 3)\%$ more positrons

Figure 9.13 shows the energy spectra of the delayed secondaries. The energy of the delayed electrons ranges up to 10 MeV. The energy spectra of the delayed photons with neutron capture in Xenon indicates the presence of two capture lines from ^{132}Xe (667.72 and 6466.07 keV), the most frequent as we have seen before, as well as a high 511 keV peak (because it is due in part to the annihilation of positrons created by capture gammas). Moreover, it should be noticed again the presence of the 2.2 MeV (neutron capture in Hydrogen) as well as the 7.9 MeV (in Copper).

A comparison between the energy distributions of electrons and photons, delayed and not, with and without neutron capture, has been done and shows the contribution of the neutron capture in the kinetic energy of all, as it is shown in Fig. 9.14.

Fig. 9.15 gives an idea of the topology of the tracks in the scored volume of TRD, as well as their spiral direction due to the magnetic field. The tracking topology of electrons and muons seems to indicate a significant difference. In fact, the momentum of the electrons is of the order of hundreds of keV/c compared with that of muons which are coming from pion decays and is hundreds of MeV/c. Therefore, electrons are curled around the magnetic field having trajectory which is a much closer helix compared with that of muons.

In the ‘detailed’ TRD response simulation as implemented in AliRoot , charged particles losing energy in the chamber gas produce primary and secondary electrons from ionization. Each electron produces a ‘hit’ from which the digitized signal for every pad is derived.

As stressed above, the geometry simulated with FLUKA has a less detailed description of the layout. In fact, there are no pads at all. Thus, it has been necessary to find a ‘virtual’ segmentation and define pads as volumes inside the scored gas layers that are in accordance with the almost rectangular shape of the real ones.

The procedure that was followed is:

- We define in the TRD layer a volume of the average area of a pad ($7.25 \times 87.5 \text{ mm}^2$) and the length in the drift direction of 0.3 cm. This volume is attached to the first ‘hit’ of an electron and any additional hit in this volume from this electron is not counted. In this way it is counted, how many such volumes are occupied by signal.
- We add the time distributions of the delayed electrons from 6 FLUKA events (sum $\sim 1281940 \text{ e}^-$ or $\sim 213000 \text{ e}^-$ per event) that fulfill the previous statement.
- We fit the final time spectra with a sum of exponential functions as

shown in Fig. 9.16.

- We do the right normalization (every function should be multiplied by $dN/dy / 6 \times 8000$), assuming 8 kHz interactions and adding randomly each of them in a histogram with bins-size= $3 \mu s$ with an average $dt \sim 125 \mu s$.
- We superimpose all of them in the same histogram for about 8500 interactions which correspond to 1 s.

Figure 9.17 shows the TRD background in both cases, including and not in the simulation the neutron capture in Xenon. From this histogram we extract the average number of hits in a $3 \mu s$ window. In addition, we estimate the number of extra hits due to the neutron capture in Xenon by subtracting the 2 distributions.

Applying the same procedure we estimate the total number of hits from all the electrons independent of their age in order to find out the contribution of the background.

The distribution of hits from all electrons and from the delayed electrons (background) in a $3 \mu s$ window as well as the distribution of the extra hits from delayed electrons due to neutron capture in Xenon are shown in Fig 9.18.

9.3.5 Results and conclusions

The results can be summarized as follows :

- Random e^- -background : ~ 1856 hits/layer/ $3\mu s$ (RMS=907)
- Random e^- -background without neutron capture in Xenon : ~ 1457 hits/layer/ $3\mu sec$ (RMS=494)
- Electron hits due to neutron capture in Xe : ~ 398 extra hits/layer/ $3\mu s$ (RMS=480)
- All electron hits : ~ 7074 hits/layer/ $3\mu s$ (RMS=15450)

→ The contribution of the background to the total number of hits (from e^-) is $\sim 26\%$ and of the neutron capture less than 6%

The number of extra hits per layer is a broad distribution with a mean value at 398 hits/layer/ $3\mu s$ and a rms of 480 hits. So most of the events will have less than 1000 extra hits/layer/ $3\mu s$. In some rare cases (two or more consecutive central events) this can go up to 4000/layer/ $3\mu s$.

Using a ‘current’ estimator for counting particles by taking into account only the first ‘hit’ position in the TRD, we estimate the number of ‘unique’ electrons that are crossing or are created in that region. The radial distribution of their origin is shown in Fig. 9.19.

The momentum spectra of all electrons as well as of the delayed (background) and of those that are produced in the gas with and without activating the neutron capture in Xenon during one central Pb-Pb collision, are shown in Fig. 9.20.

Applying the same procedure as before we estimate the number of the ‘unique’ delayed secondaries in $3\mu s$ window:

Number of delayed particles in the TRD in a $3\mu s$ window

- Electrons : $\sim 264 e^-$ /layer/ $3\mu sec$ (RMS=144)
- Photons : $\sim 9750 \gamma$ /layer/ $3\mu sec$ (RMS=4434)
- Neutrons : $\sim 43500 n$ /layer/ $3\mu sec$ (RMS=42000)
- Positrons : $\sim 12 e^+$ /layer/ $3\mu sec$ (RMS=6)

Without activating the neutron capture in Xenon the delayed ‘unique’ particles are:

Number of delayed particles in the TRD in a $3\mu s$ window

- Electrons : $\sim 195 e^-$ /layer/ $3\mu sec$ (RMS=63)
- Photons : $\sim 7848 \gamma$ /layer/ $3\mu s$ (RMS=2643)
- Positrons : $\sim 9 e^+$ /layer/ $3\mu s$ (RMS=3)

To conclude, the total number of hits in a central Pb–Pb collision in a $3 \mu\text{s}$ window is a broad distribution with a mean of 7074 hits/layer and an rms of 15450/layer. Of these the random steady-state background contributes 26% as it produces extra hits in the Xe readout chambers with a mean of 1856 hits/layer and an rms of 907/layer. The neutron capture in Xe has as result a 22% increase in the background and a 6% increase in the total number of hits.

The results show that the n-capture in Xe does not increase the background by a big amount but it is not negligible and will be included in the AliRoot simulations.

9.4 Radioactivity in the gas system of ALICE TRD

Due to the high neutron and charged particle fluxes at the ALICE TRD, it is very probable to have radioactive isotopes produced from the circulating gas used in the detector. Depending on the lifetime of the isotope produced, the resulting activity may be quite high, and should be taken into account particularly during the run period, because part of the gas is supposed to be always in accessible areas.

An estimate of the activity levels of the TRD gas system is presented in comparison with CERN safety limits, based on a similar study which was done for ATLAS-ID-TRT [146].

9.4.1 Calculation of activity

Radioactive isotopes can be produced by many reactions like (n,γ) , $(n,2n)$, (π,p) etc. Among them, neutron capture process has the highest significance for the TRD gas activation because of its large cross section at low neutron energies.

Activity is defined as the number of decays per second, but the specific activity, which takes into account the number of particles emitted per decay, is considered here. The specific activity A can be calculated as:

$$A = \Phi \cdot \sigma \cdot N \cdot M \cdot X \cdot (\text{buildup}) \cdot (\text{decay}) \quad (9.1)$$

Where: Φ is the neutron flux (kHz/cm²), σ is the neutron capture cross-section (10²⁴ barn), N is the number of parent atoms per unit mass (atoms/g), M is the mass of element considered (g), and X is the number of particles emitted per decay. The effect of build-up and decay are calculated as:

$$(\text{buildup}) = 1 - e^{-\lambda \cdot T} \quad (9.2)$$

$$(\text{decay}) = e^{-\lambda \cdot t} \quad (9.3)$$

where $\lambda = (\ln 2)/T_{1/2}$, $T_{1/2}$ is the half-life, T is the irradiation time (a maximum running time of 100 days per year is assumed at the LHC), and t is the decay time (the rest of the year ~ 250 days). The build-up factor determines how many isotopes of our interest are produced during the irradiation time which is the run period taken as 100 days for a year. When the beam is off, the decay factor calculates the number of decays for the rest of the year.

The standard unit of activity is Becquerel (Bq) which is the number of particles per second. Relation between often used Curie (Ci), and Becquerel is $1 \text{ Ci} = 3.7 \times 10^{10} \text{ Bq}$ (or $3.7 \times 10^{10} \text{ sec}^{-1}$). The product of the absorbed dose in tissue due to radiation, so called the dose equivalent, is expressed in units of Sievert (Sv: $1 \text{ Sv} = 1 \text{ J/kg}$).

There are two types of decays which should be considered separately, gamma and beta decays. For the gamma decays, so called “gamma exposure factor” (also known as the specific gamma constant) should be taken into account. It relates the activity of a point source with a certain energy to the dose equivalent at a distance. The equivalent dose from $1 \mu\text{C}$ point source at a distance of D meters is $\Gamma/D^2 \mu\text{Sv/h}$ [147, 148]. The CERN safety limits for gamma radiation [149] are summarised in Table 9.8.

Table 9.8: CERN safety limits for gamma radiation.

AREA	MAX DOSE RATE ($\mu\text{Sv/h}$)
NON-DESIGNATED	<0.5
SUPERVISED	<7.5
SIMPLE CONTROLLED	<100

In the ATLAS-TRT study, it is shown that from all the possible radioactive products only Xe has large neutron capture cross-section and should be considered as potentially dangerous element. In calculations, isotopes with cross-sections less than 10^2 barn, or with lifetimes less than a few minutes were ignored (assuming ~ 10 minutes minimum for gas to travel from detector to accessible areas). Beta activity of Xenon was not taken into account because the minimum thickness of any gas system wall is 0.5 mm of stainless steel which will very effectively attenuate the radiation.

The gamma activity of each isotope was calculated separately for 1 kg of the bulk material, so that it is easy to estimate the total activity by scaling to the amount of the material to be used. Summing the activities of all isotopes, at the end of the running period (100 days), it was calculated that for 1 kg of Xenon, activated by slow neutrons, the maximum activity is ~ 0.4 mCi. It was also shown that 6% of the photons have energies above 250 keV and 0.5% above 550 keV.

9.4.2 Scaling ATLAS results to ALICE TRD

The ATLAS SCT aims to operate reliably according to performance specifications over a 10-year period of high luminosity LHC operation. The design LHC luminosity aims for an average peak value of $10^{34} \text{ cm}^{-2}\text{s}^{-1}$ over 10^7 secs per year, giving an annual integrated luminosity of 10^{41} cm^{-2} . Instantaneous rates may exceed this value. These luminosities are achieved using bunch-bunch crossings separated by 25 nsec (40MHz) to result in a particle interaction rate $\sim 10^9$ Hz [150]. The standard running scenario for

particle production in ATLAS and in ALICE respectively, is summarized in Table 9.9

The neutron flux values used throughout the ATLAS study were taken from reference [151].

$$\rightarrow \text{Neutron Fluence} \sim 8 \times 10^{13} [\text{particles}/\text{cm}^2/\text{year}]$$

$$\rightarrow \text{Thermal neutron Fluence} \sim 3 \times 10^{13} [\text{particles}/\text{cm}^2/\text{year}]$$

Table 9.9: Operational scenario for a one year running period ($\langle L \rangle$ stands for mean luminosity and σ_t for inelastic cross section.)

	ATLAS pp	ALICE PbPb
$\langle L \rangle [\text{cm}^{-2}\text{s}^{-1}]$	10^{34}	10^{27}
$\sigma_t[\text{b}]$	0.07	8
Rate $[\text{s}^{-1}]$	10^9	8×10^3
Runtime [s]	10^7	5×10^5
Events/year	10^{16}	4×10^9

According to Eq. 9.1, the specific activity A is proportional to the neutron flux. Assuming for simplicity that the running period is the same, the aforementioned activity of 1 kg of Xenon can be scaled in accordance with the neutron fluence in ALICE TRD as summarized in Table 9.7.

Thus, for 1 kg of Xenon, activated by slow neutrons, the maximum activity is $\sim (0.04-0.1) \mu\text{Ci}$ in ALICE TRD. The volume of the TRD is $\sim 27 \text{ m}^3$. Assuming the worst scenario that 150 kg of Xenon are stored in a cylindrical container with dimensions length=4×diameter, the maximum radiation dose is about $2.3 \mu\text{Sv/h}$ on the surface. Since this value is already below the supervised area limit of $7.5 \mu\text{Sv/h}$, no special shield is required.

9.4.3 Conclusions

The resulting activity and dose rate of Xenon appear to be rather low and safe, especially if compared with the expected general radiation environment. All parts of the TRD gas system have rates below supervised limit

and no special shielding is required. The possible leakage of Xenon into the ALICE cavern does not lead to any safety problems.

9.5 Estimation of the radiation level in the ALICE TPC electronics

The inaccessibility of the ALICE experiment during the entire year of LHC running makes stringent quality tests of the readout electronics mandatory before installation. Here we analyze and present the contributions to the radiation background in the region where the ALICE TPC front-end electronics is situated. The simulations were based on the FLUKA interaction and transport Monte Carlo code.

The Time Projection Chamber (TPC) [154] surrounds the Inner Tracking System (ITS) and is the main tracking detector of the central barrel and together with the ITS, TRD and TOF will provide charged particle momentum measurement, particle identification and vertex determination with sufficient momentum resolution, two track separation and dE/dx resolution for studies of hadronic and leptonic signals in the region $P_t < 10$ GeV/c and pseudorapidities $|\eta| < 0.9$. To cover this acceptance the TPC is of cylindrical design with an inner radius of about 80 cm, an outer radius of about 250 cm and an overall length in the beam direction of 500 cm. A gas mixture of 90% Ne, 10% CO₂ has been chosen for operating the detector. The front-end electronics read out the charge detected by about 570 000 cathode pads located on the readout chambers at the TPC end-plates. Using the FLUKA geometry, we define 4 concentric cylindrical layers of silicon at radial distances from 77.2 up to 278.17 cm with 1 mm width along the beam direction, 10 cm away from the TPC limiting planes. We perform two studies for both end-plates (μ -absorber and non-absorber side). Events with average multiplicity of 80 000 primary pions and kaons were transported through the material of the experiment and experimental area which was described with about 3200 volumes. The neutron fluence in the first Si layer (nearest to the beam axis) in particles/cm²/primary per cen-

Table 9.10: Particle fluences with $E_{\text{kin}} > 10$ MeV and total absorbed doses per 10 ALICE years .

Scoring region	μ -absorber side	non-absorber side
n [cm^{-2}]	$(2.4-8.4) \times 10^9$	$(1.1-2.8) \times 10^9$
p [cm^{-2}]	$(1.2-3.2) \times 10^8$	$(1.1-4.8) \times 10^8$
π [cm^{-2}]	$(0.7-1.4) \times 10^9$	$(0.8-2.9) \times 10^9$
k [cm^{-2}]	$(2.4-7.6) \times 10^7$	$(3.3-19.3) \times 10^7$
Total Dose [Gy]	(0.8-2.5)	(0.3-5.7)

tral event is: $(3.42 \times 10^{-5}) \pm 1.6\%$ and $(1.27 \times 10^{-5}) \pm 1.3\%$ for μ -absorber and non-absorber side respectively, as is shown in Fig. 9.21.

To scale up to a ten-year run period we multiply the aforementioned result of the fluence per central event with a factor of 3.2×10^{15} (80000 primaries \times 8 KHz / $5 \times 2.5 \times 10^6$ sec/year \times 10 years).

The radiation load on the TPC electronics is relatively low, with a neutron flux received over 10 years of $(0.6-1.1) \times 10^{11}$ neutrons/ cm^2 . Thus, standard radiation-soft technologies are suitable for the implementation of this electronics. Nevertheless, some special care should be taken to protect the system against potential damage caused by Single Event Effects (SEEs). Concerning the SEU (Single Event Upset) in the FPGAs probably only the protons above 10-20 MeV can cause bit-flips. Neutrons can contribute to this effect only if they scatter in the plastic of the chip package or in the PCB with a proton and kick the fast proton into the silicon.

The particle fluences with $E_{\text{kin}} > 10$ MeV in both sides of TPC are summarized in Table 9.10.

The aforementioned results of this study [153] concerning the particle rates, fluences and fluxes should be taken into account for evaluating the radiation tolerance of the TPC electronics.

All the study including more details can be found in appendix C.

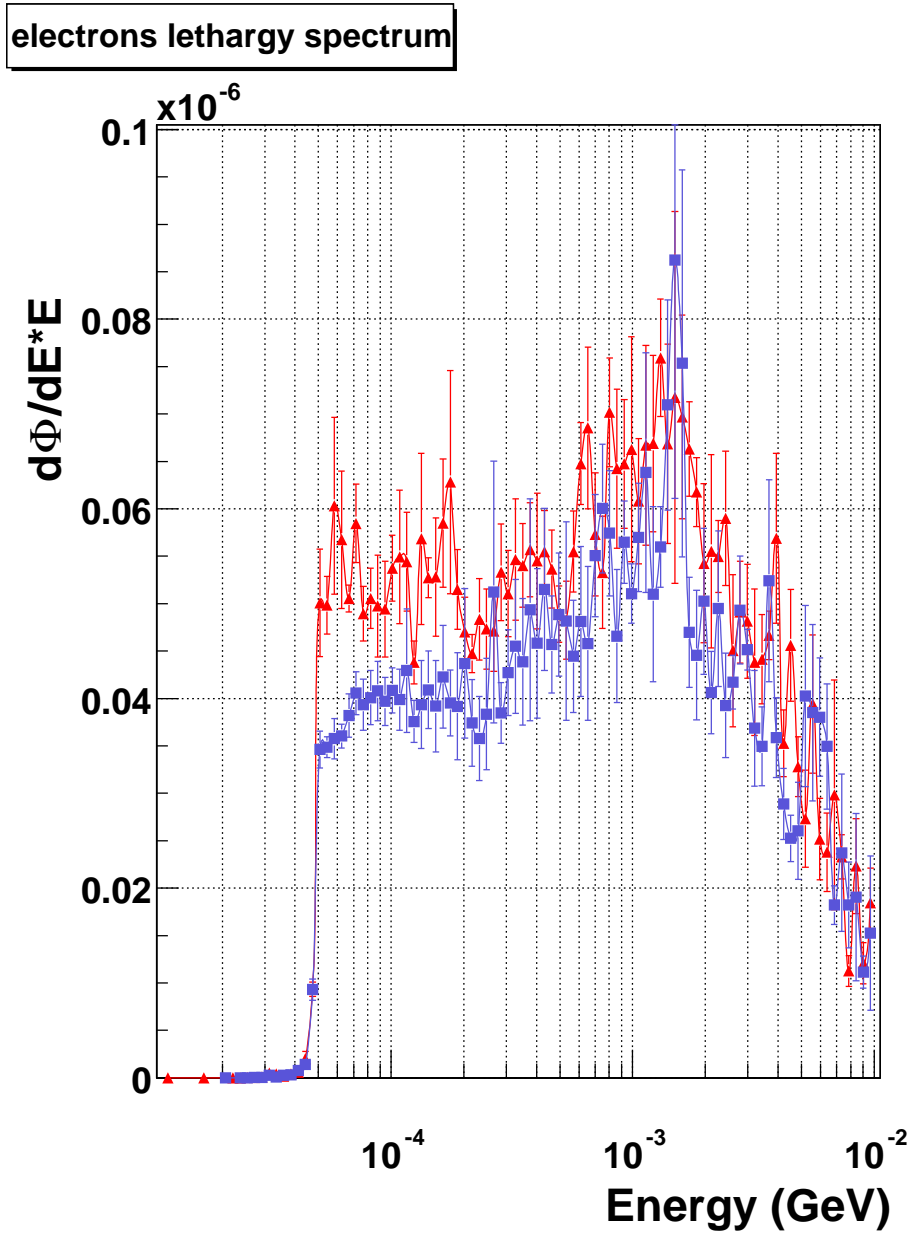


Figure 9.7: Electron fluence spectra in one Xenon layer during one FLUKA event, whereas the red curve (full triangle) has been taken with activated the neutron capture in Xenon and the blue curve (full rectangle) without.

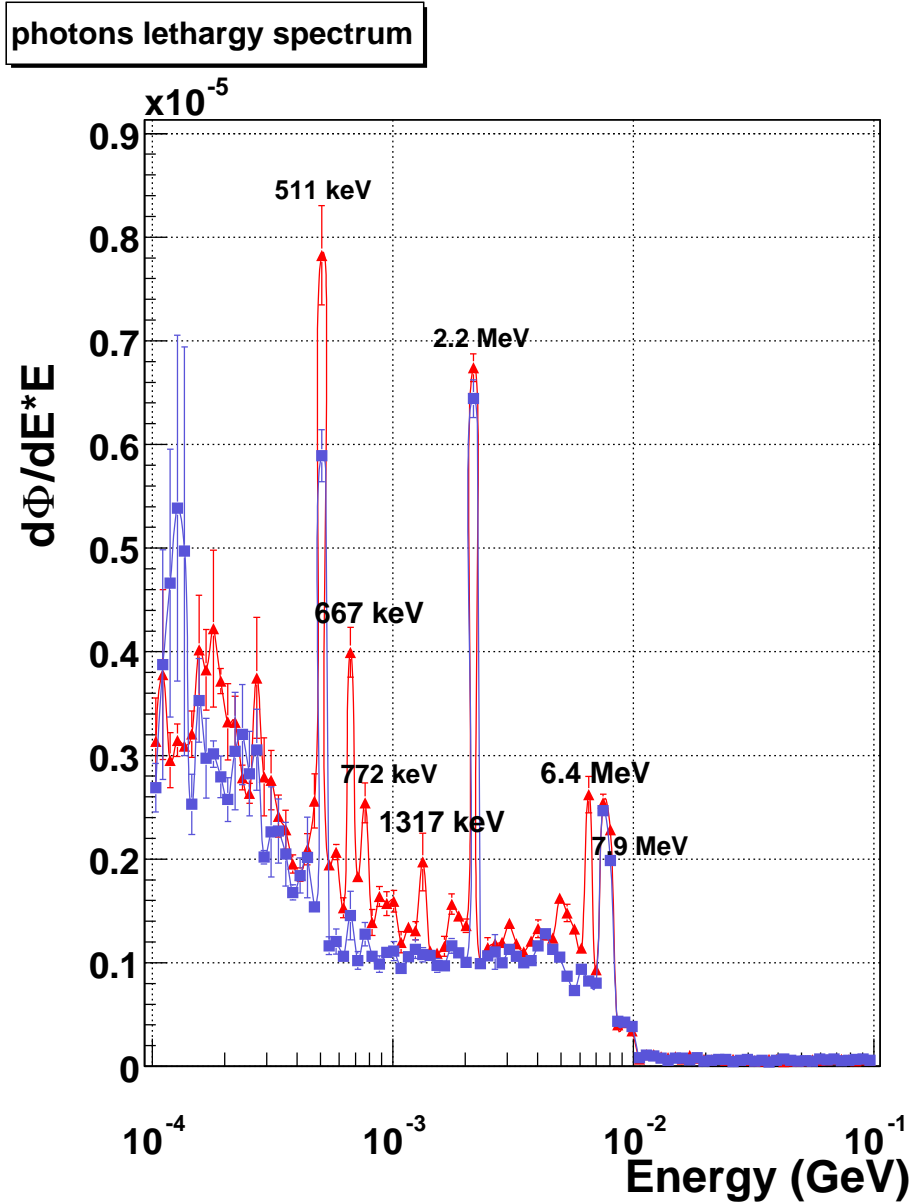


Figure 9.8: Photon fluence spectra in one Xenon layer during one FLUKA event, whereas the red curve (full triangle) has been taken with activated the neutron capture in Xenon and the blue curve (full rectangle) without.

neutrons lethargy spectrum

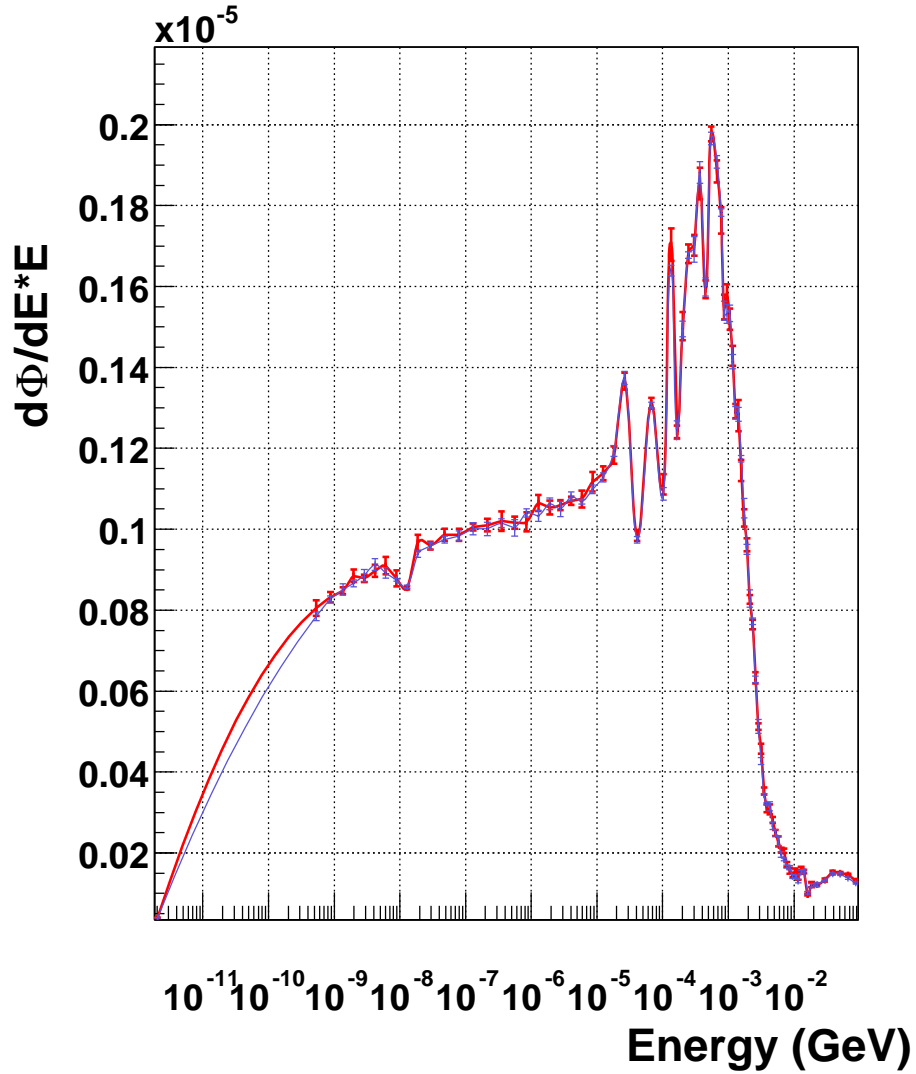


Figure 9.9: Neutron fluence spectra in one Xenon layer during one FLUKA event, whereas the red curve has been taken with activated the neutron capture in Xenon and the blue curve without.

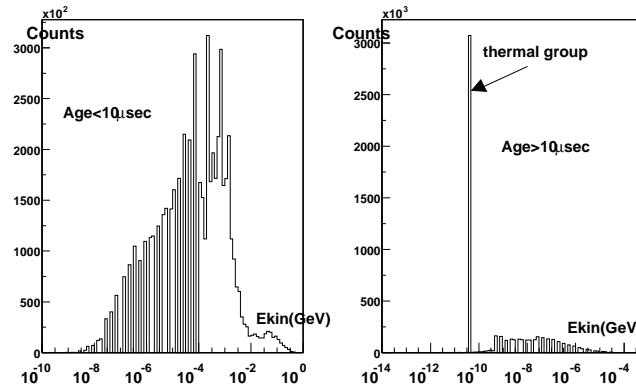


Figure 9.10: Energy spectra of neutrons.

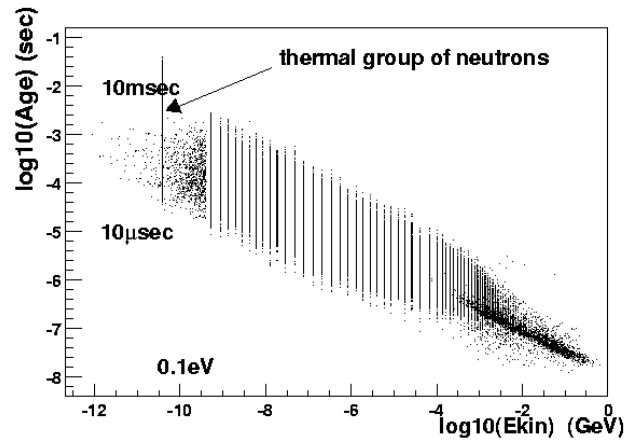


Figure 9.11: Age-Energy distribution of neutrons.

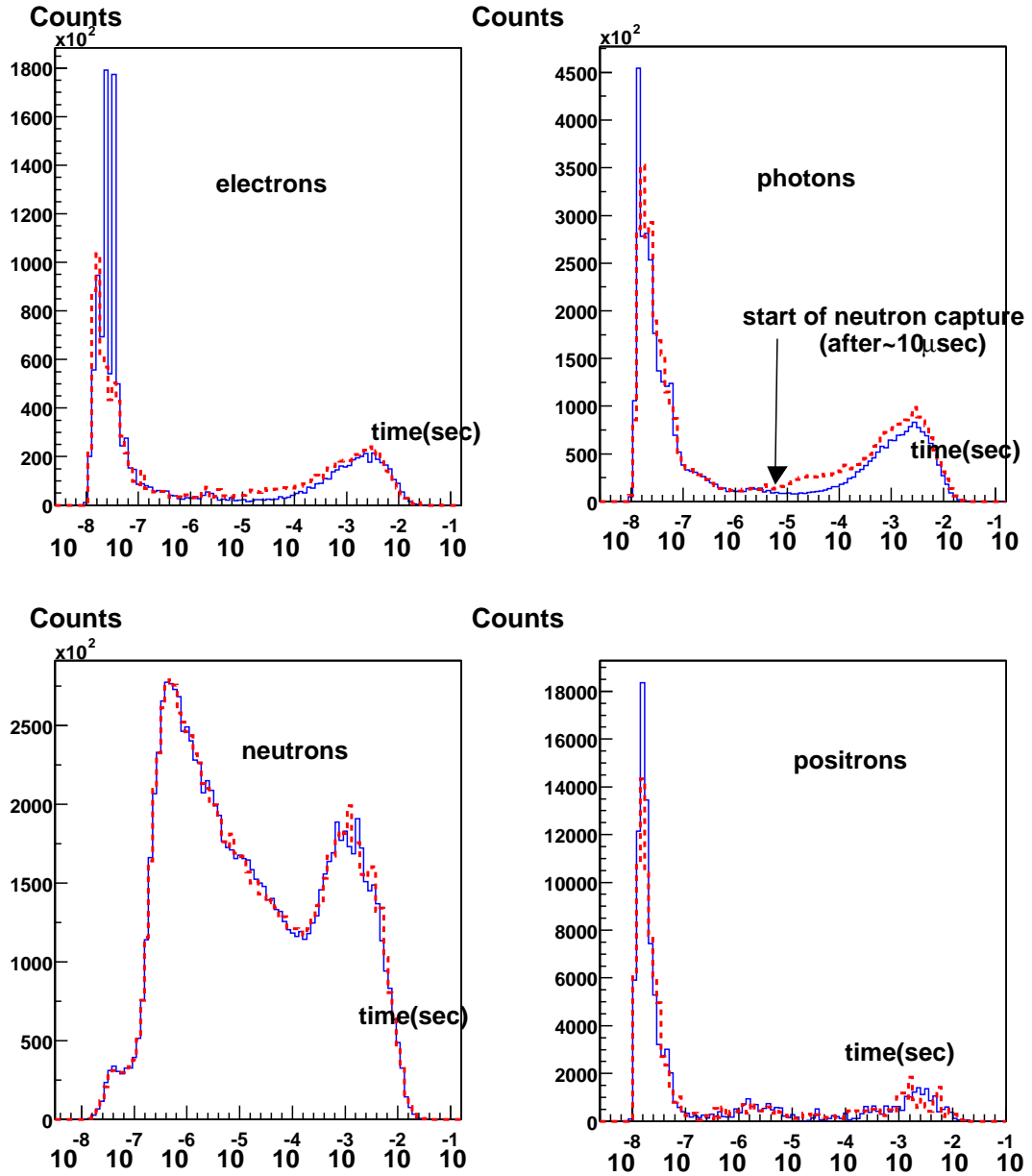


Figure 9.12: Time Spectra of e^- , γ , n and e^+ . The red curves (dashed line) are taken by one event with activated the neutron capture in Xenon. The blue (solid line) without.

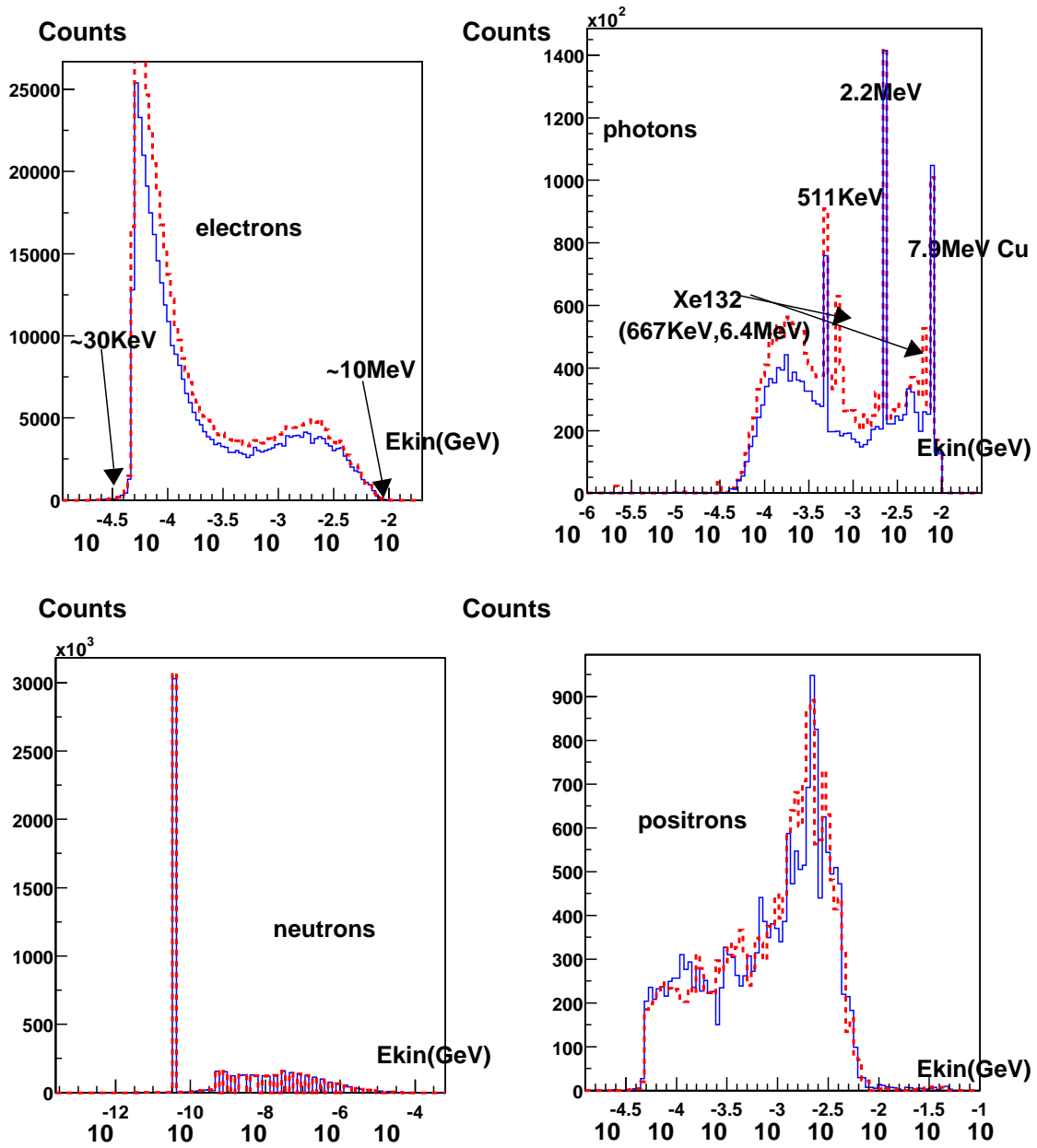


Figure 9.13: Energy Spectra of e^- , γ , n and e^+ . The red curves (dashed line) are taken by one event with activated the neutron capture in Xenon. The blue (solid line) without.

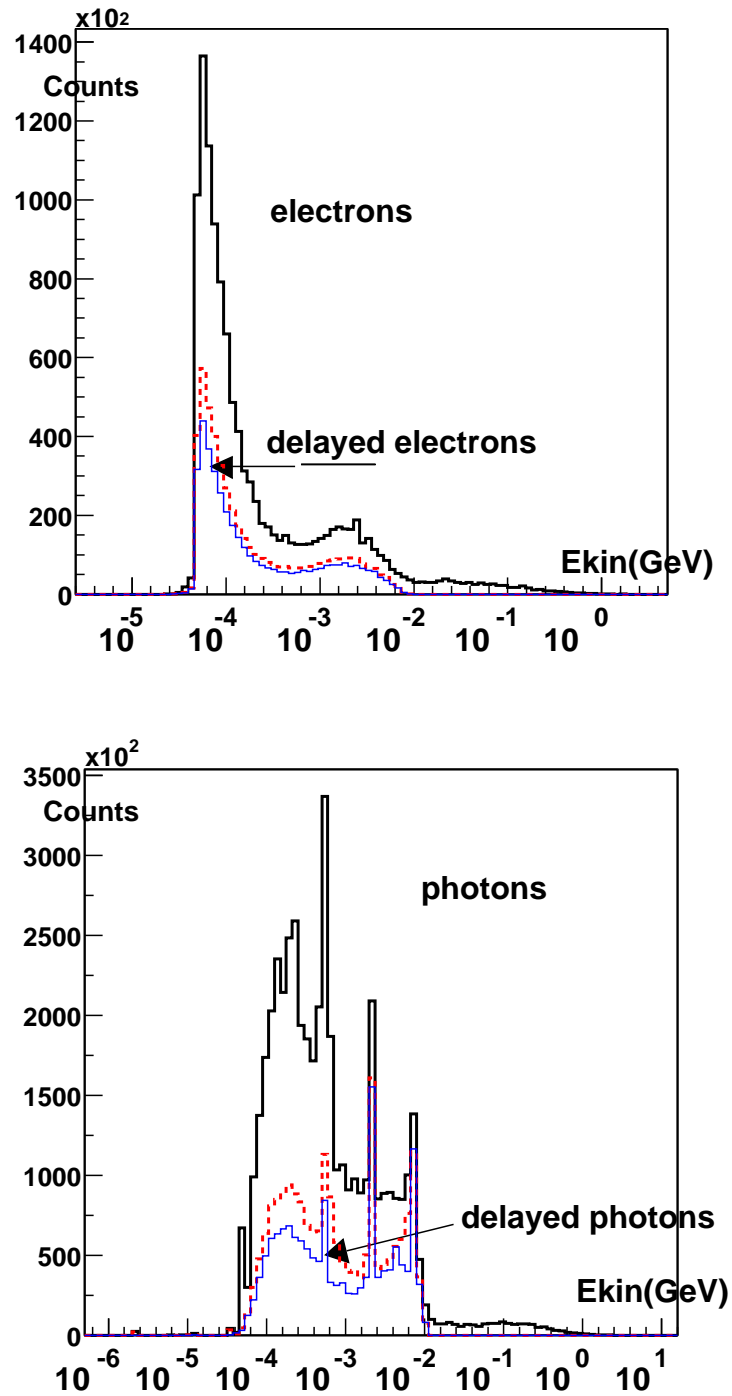


Figure 9.14: Energy Spectra of delayed e^-,γ compared with the Spectra of all e^-,γ respectively during one FLUKA event. The red curves (dashed line) are taken by one event with activated the neutron capture in Xenon. The blue (solid line) without.

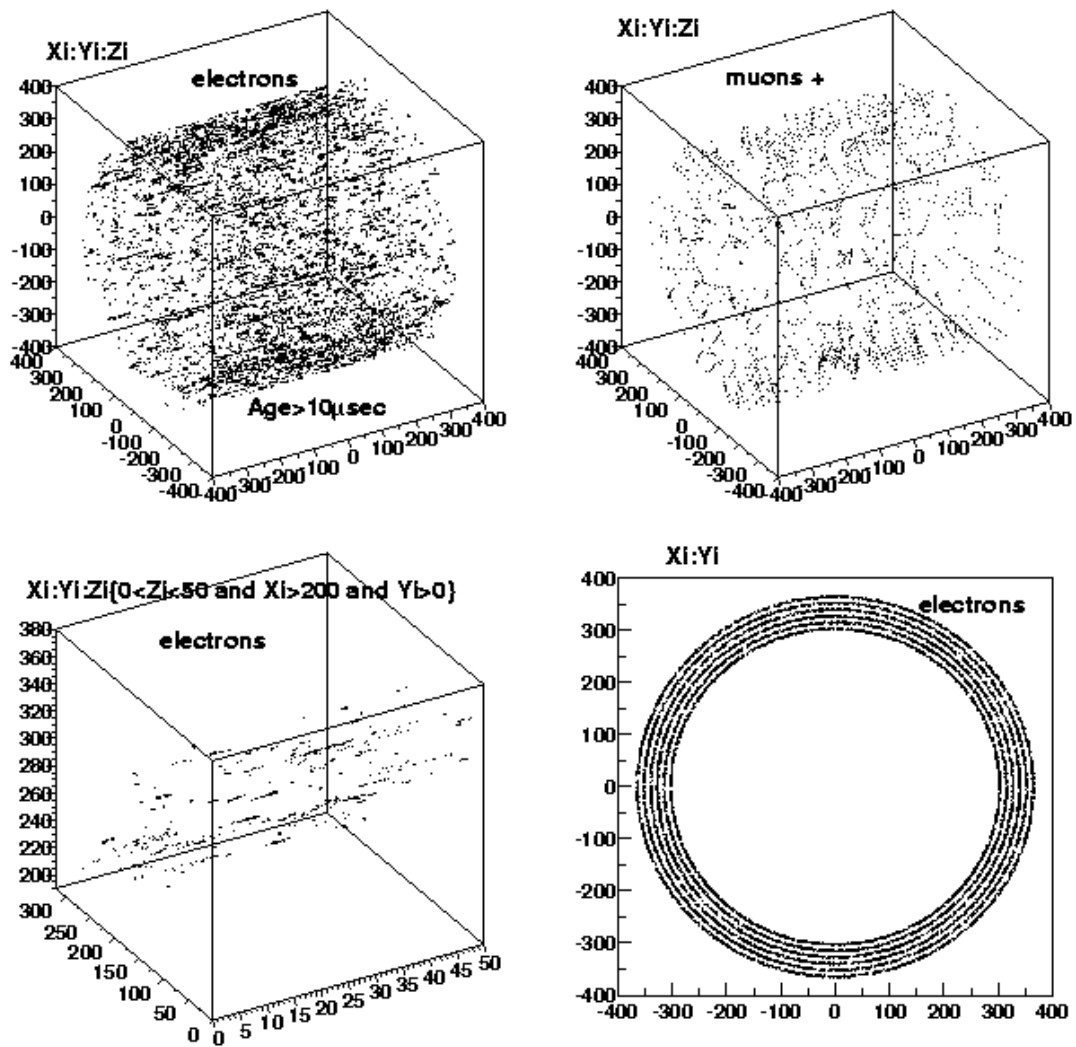


Figure 9.15: Topology of the tracks for e^- and μ^+ respectively.

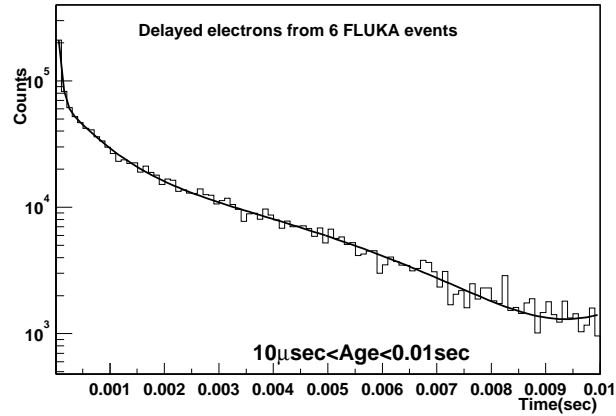


Figure 9.16: The time spectrum of the delayed electrons. The line is a fit with a sum of exponential functions.

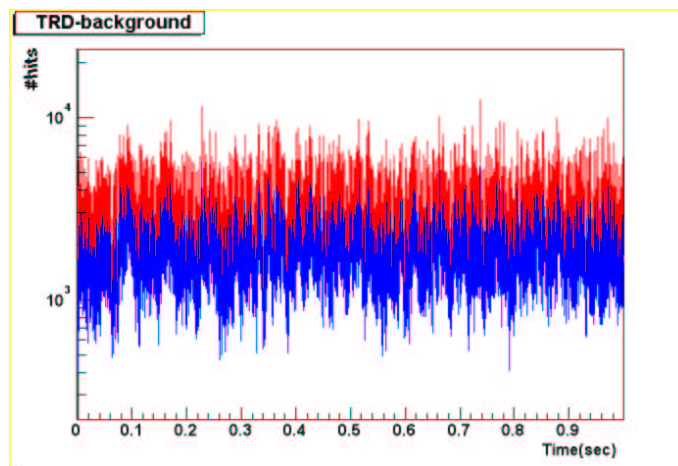


Figure 9.17: TRD-background, where the red shows the fluctuations of the hits with activated the neutron capture in Xenon and the blue without.

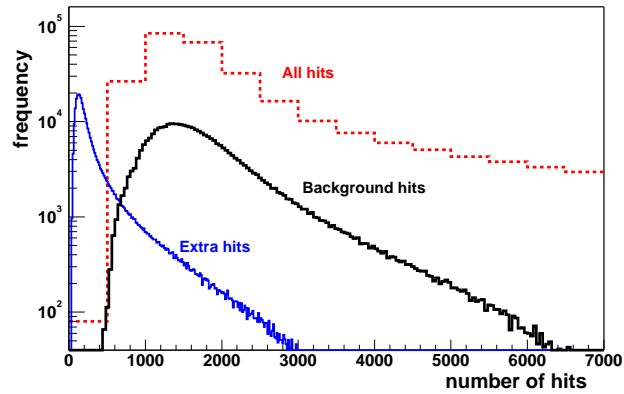


Figure 9.18: The distribution of the number of hits from all e^- and delayed e^- (background) and extra hits (from delayed e^-) in a $3\mu s$ window due to neutron capture in Xenon.

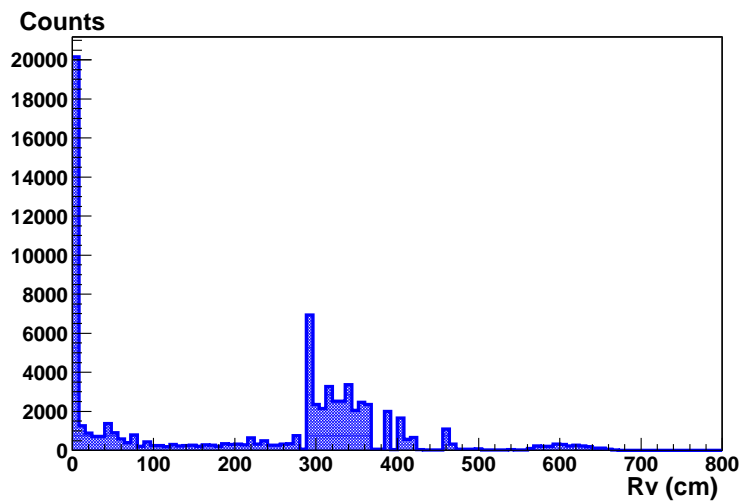


Figure 9.19: Radial distribution of all 'unique' electrons origin that scored in the TRD gas layers

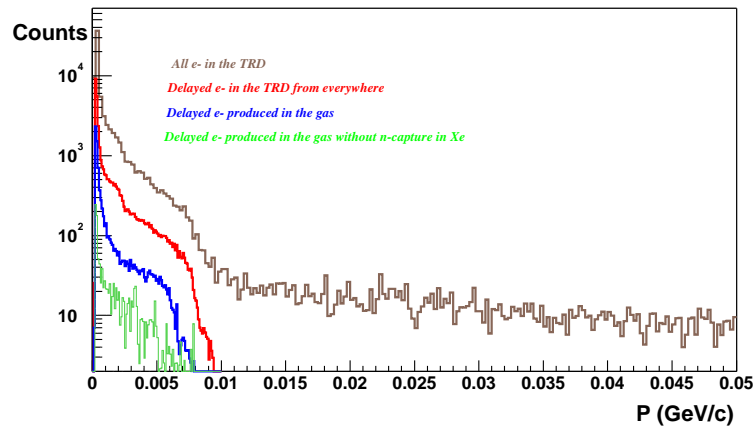


Figure 9.20: Momentum spectra of 'unique' electrons in the TRD

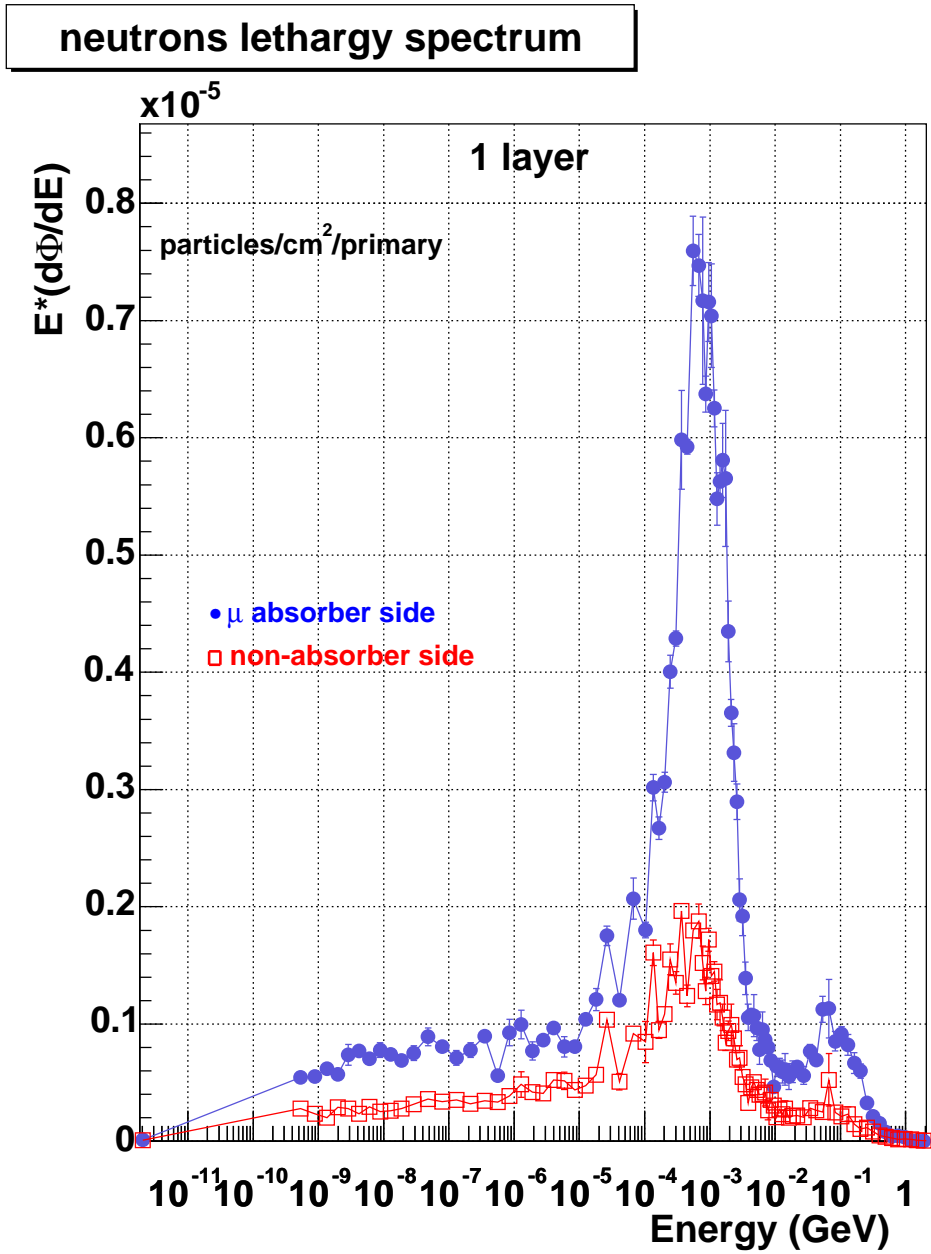


Figure 9.21: Lethargy energy spectra of neutrons in the μ -absorber (full circles) and non-absorber side (empty rectangles) of the TPC (one central event).

Appendix A

Two-particle correlation plots

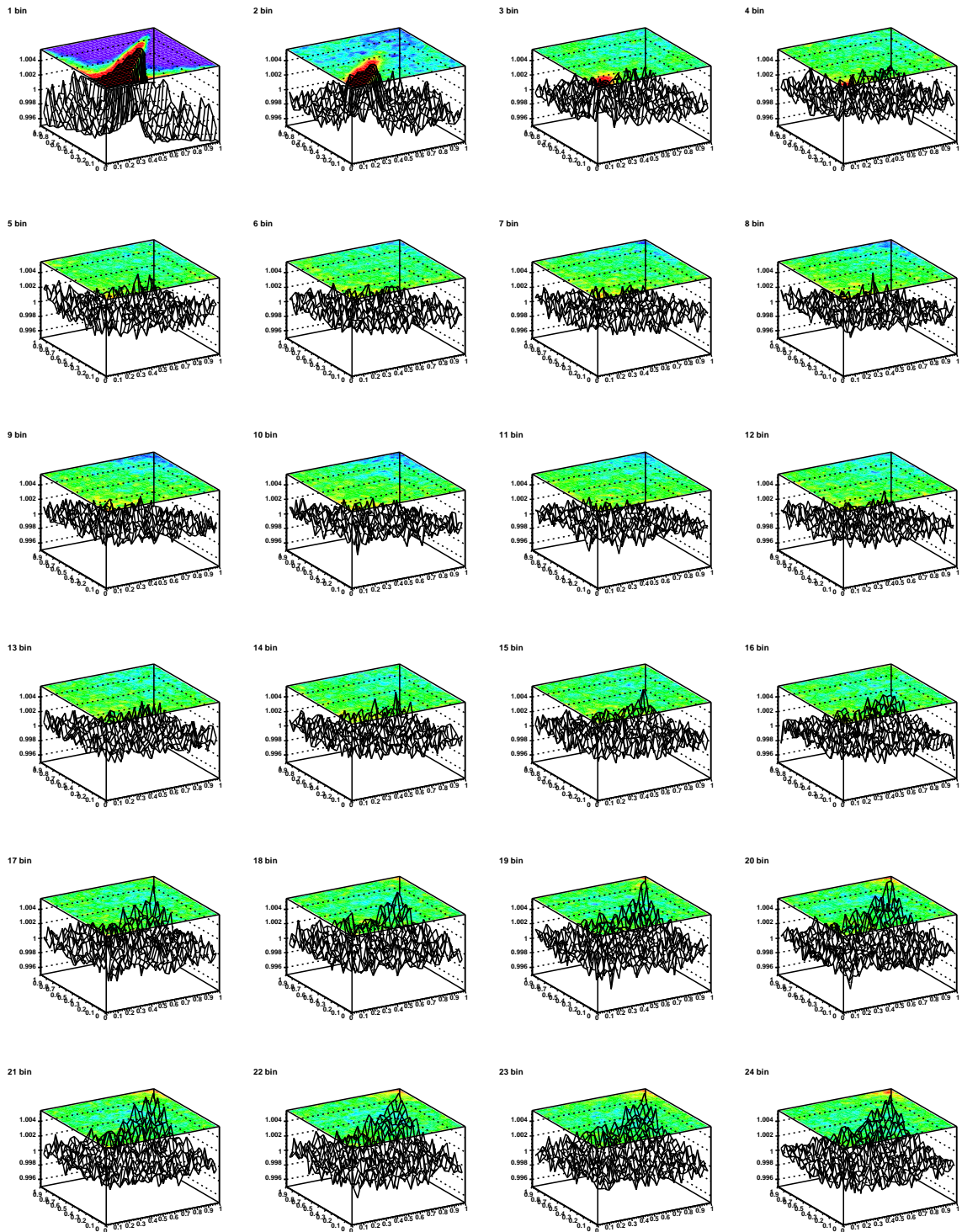


Figure A.1: Two-particle correlation plots using the cumulant p_T variable x for all pairs, in several $\Delta\phi$ regions.

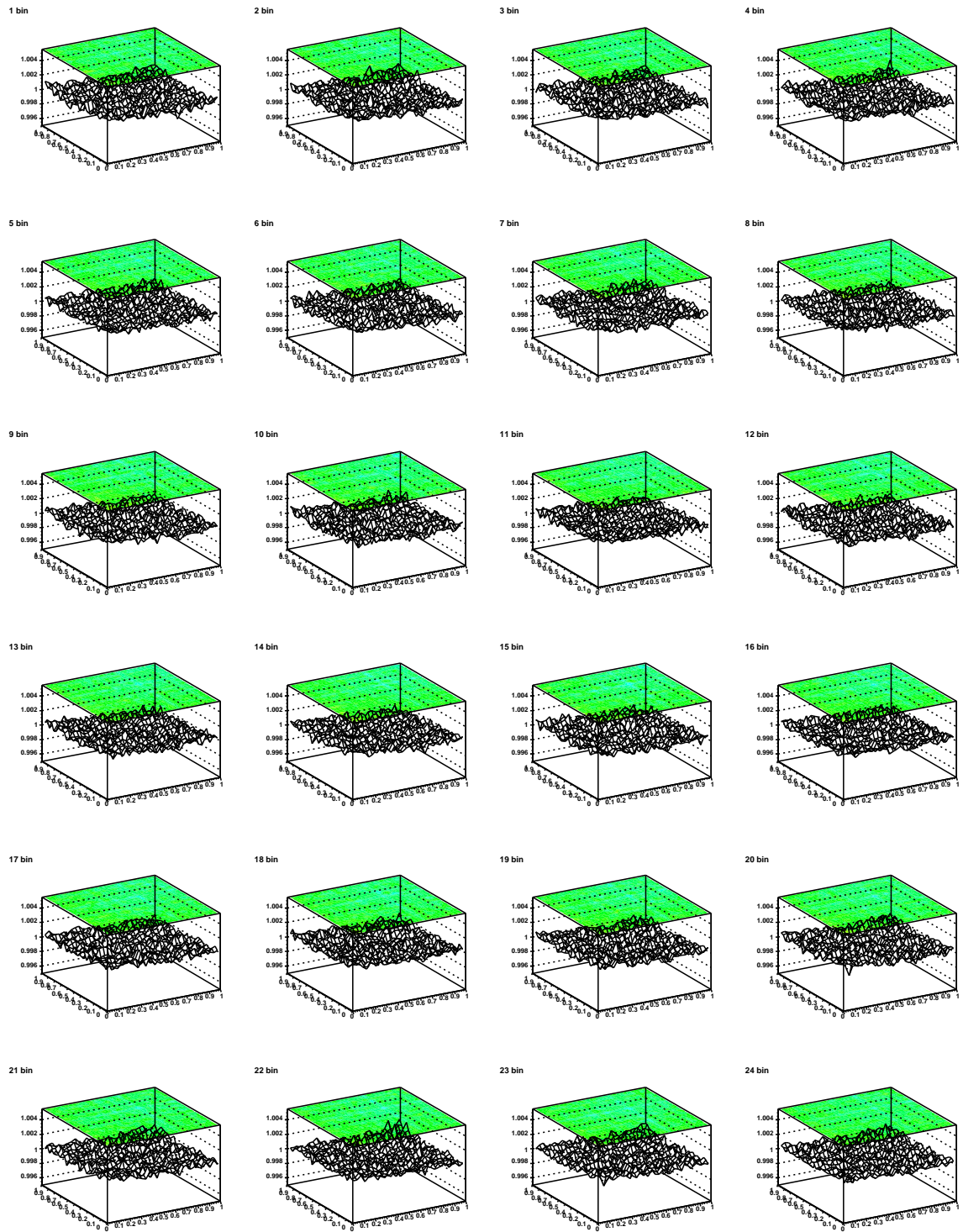


Figure A.2: Two-particle correlation plots using the cumulant p_T variable x for all pairs that have only the elliptic flow expected by CERES (corrected by dividing mixed with flow versus mixed), in different $\Delta\phi$ regions.

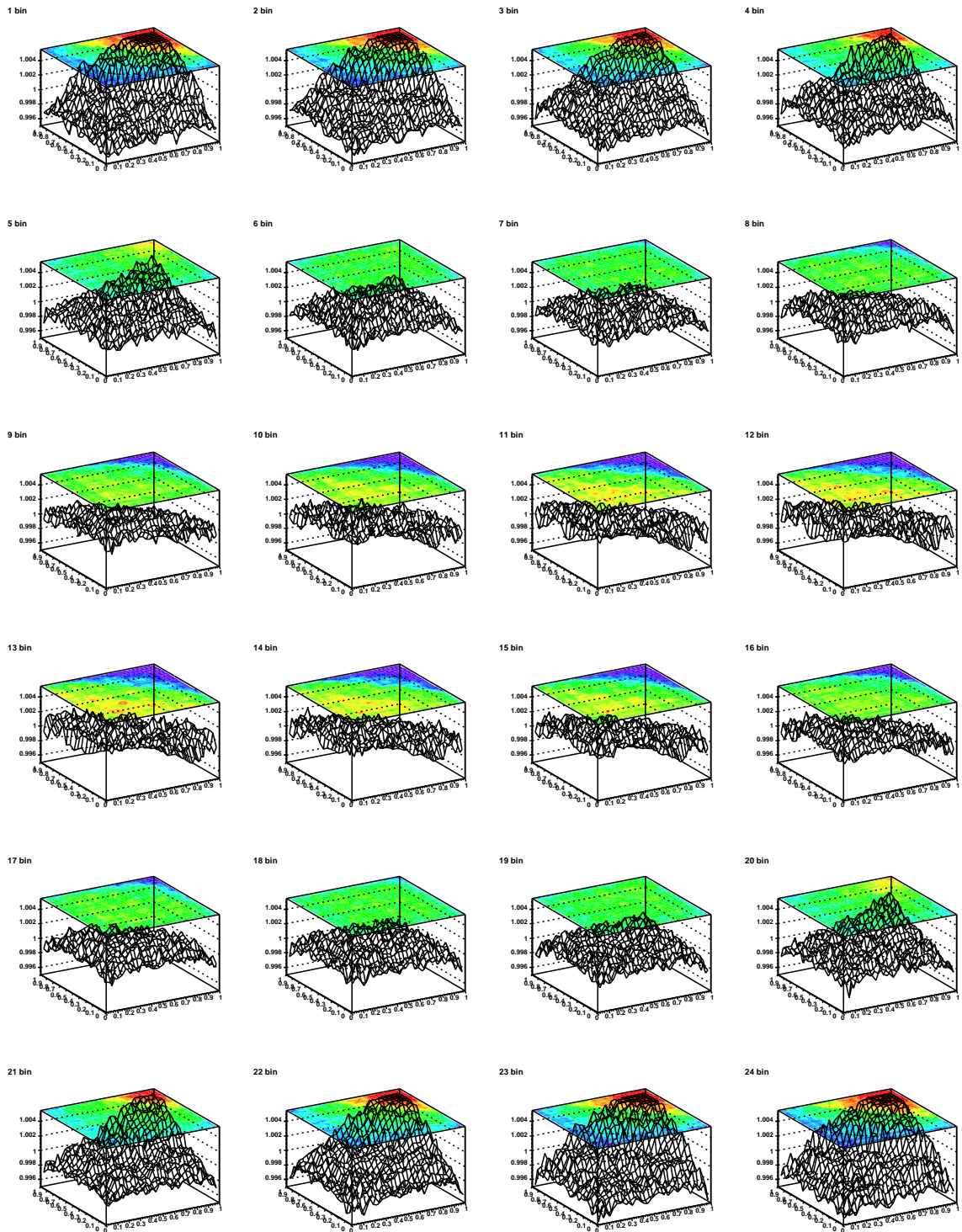


Figure A.3: Two-particle correlation plots using the cumulant p_T variable x for all pairs that have only elliptic flow with $3v_2$, where v_2 gets the expected by CERES value (corrected by dividing mixed with flow versus mixed), in several $\Delta\phi$ regions.